SANDIA REPORT
SAND2009-6133
Unlimited Release
Printed September 2009

Low Impedance Z-Pinch Drivers Without Post-Hole Convolute Current Adders

David B. Seidel, Clifford W. Mendel, Jr., and Mark E. Savage

Prepared by
Sandia National Laboratories
Albuquerque, New Mexico 87185 and Livermore, California 94550

Sandia is a multiprogram laboratory operated by Sandia Corporation,
a Lockheed Martin Company, for the United States Department of Energy's
National Nuclear Security Administration under Contract DE-AC04-94AL85000.

Issued by Sandia National Laboratories, operated for the United States Department of Energy by Sandia Corporation.

Available to DOE and DOE contractors from
U.S. Department of Energy
Office of Scientific and Technical Information
P.O. Box 62
Oak Ridge, TN 37831

Telephone: (865) 576-8401
Facsimile: (865) 576-5728
E-Mail: reports@adonis.osti.gov
Online ordering: http://www.osti.gov/bridge

Available to the public from
U.S. Department of Commerce
National Technical Information Service
5285 Port Royal Rd.
Springfield, VA 22161

Telephone: (800) 553-6847
Facsimile: (703) 605-6900
E-Mail: orders@ntis.fedworld.gov
Online order: http://www.ntis.gov/help/ordermethods.asp?loc=7-4-0#online

SAND2009-6133
Unlimited Release
Printed September 2009

Low Impedance Z-Pinch Drivers Without Post-Hole Convolute Current Adders

David B. Seidel and Clifford W. Mendel, Jr.*
Advanced Pulsed Power Systems Department

Mark E. Savage
Advanced Accelerator Physics Department

Sandia National Laboratories
P.O. Box 5800
Albuquerque, New Mexico 87185-1152

Abstract

Present-day pulsed-power systems operating in the terawatt regime typically use post-hole convolute current adders to operate at sufficiently low impedance. These adders necessarily involve magnetic nulls that connect the positive and negative electrodes. The resultant loss of magnetic insulation results in electron losses in the vicinity of the nulls that can severely limit the efficiency of the delivery of the system's energy to a load. In this report, we describe an alternate transformer-based approach to obtaining low impedance. The transformer consists of coils whose windings are in parallel rather than in series, and does not suffer from the presence of magnetic nulls. By varying the pitch of the coils' windings, the current multiplication ratio can be varied, leading to a more versatile driver. The coupling efficiency of the transformer, its behavior in the presence of electron flow, and its mechanical strength are issues that need to be addressed to evaluate the potential of transformer-based current multiplication as a viable alternative to conventional current adder technology.

* C. W. Mendel, Jr. is with Cove Consulting, Belle Haven, VA 23306 USA.

ACKNOWLEDGMENTS

The authors wish to acknowledge the contributions of Gerard Torres, who was most helpful in fielding the transformer experiments which were performed on the Tesla accelerator. We also thank Mark Kiefer and Larry Schneider, who were instrumental in championing this work, and the LDRD programming for the funding they provided to pursue it.

CONTENTS

FIGURES

TABLES

NOMENCLATURE

2D	two dimensional
3D	three dimensional
Atheta	2D cylindrical Magnetostatic coil design code developed at SNL
cm	length unit – 10^{-2} meters (SI)
EM	electromagnetic
kA	unit of electric current – 10^{3} Amperes (SI)
kJ	unit of energy – 10^{3} Joules (SI)
kV	unit of electric potential – 10^{3} Volts (SI)
MA	unit of electric current – 10^{6} Amperes (SI)
MJ	unit of energy – 10^{6} Joules (SI)
MV	unit of electric potential – 10^{6} Volts (SI)
mV	unit of electric potential – 10^{-3} Volts (SI)
MITL	magnetically-insulated vacuum transmission line
mm	length unit – 10^{-3} meters (SI)
nH	unit of inductance – 10^{-9} Henrys (SI)
ns	time unit – 10^{-9} seconds (SI)
PIC	particle in cell
PRS	plasma radiation source
Quicksilver	3D EM PIC code developed at SNL
SI	International System of Units
SNL	Sandia National Laboratories
Tesla	Small pulsed-power accelerator at SNL
Z	Low-impedance, high-current accelerator at SNL
ZR	Refurbished Z accelerator, indicating upgrade performed in 2007
μH	unit of inductance – 10^{-6} Henrys (SI)
μs	time unit – 10^{-6} seconds (SI)
Ω	Ohm, SI unit of electrical resistance

1.0 INTRODUCTION

Z-pinch radiation source drivers such as Z and ZR must supply very high currents at moderate (by pulsed power standards) voltage. This in turn requires very low inductance feeds. Presently this is accomplished by adding several higher impedance drivers in parallel using a post-hole convolute current adder. Unfortunately, current addition results in localized magnetic nulls that extend from the cathode to the anode.[1] Since the cathode surfaces emit electrons at the space-charge limit, the nulls result in electron losses. These losses are in addition to those due to magnetically insulated flow over most of the transmission lines, and, more importantly, these losses occur over small areas of the anode resulting in electrode damage and conducting gases that cause major current losses and further damage.

It is possible to replace the current adder (convolute) with a transformer that allows driver power to be combined in series with voltage adders, and then converted to lower voltage and higher current in the transformer. In contrast to common transformers, these transformers consists of coils whose windings are in parallel rather than series. These coils are similar to coils found in a number of other pulsed power devices, such as some ion diodes[2] and triggered plasma opening switches.[3]

There are several potential benefits to using a transformer approach. Such a system would have no magnetic nulls to cause localized current losses. Moreover, the current multiplication ratio can easily be varied, resulting in a more versatile driver. The critical issues that must be addressed are achieving sufficient coupling between the primary and secondary circuits, operating successfully in the presence of flow electrons, and building a primary coil with adequate mechanical strength. This report will describe the design of such a system, and will present results analyzing the performance of such a system in comparison to the standard post-hole convolute approach. As part of this project, a prototype transformer system was designed, fabricated, and fielded on the Tesla accelerator. The findings from these experiments will also be described.

1.1 Transformer Topology

Fig. 1 shows a radial plane cutaway view of a simple transformer. One-half of a primary coil and one-quarter of a secondary coil are shown in a composite drawing in Fig. 2. To give some idea of the angle subtended by the vanes, single primary and secondary vanes are shown in red and green, respectively. The lower-left quadrant of Fig. 2 also shows the radial vanes, one of which is shown in blue. In this simple transformer the two coils could be pitched in the same direction, or opposite directions as shown. The conductor between the two coils consists of radial vanes (shown in blue in Fig. 1). Radial vanes allow penetration of the *r* and *z* components of the magnetic field. The primary and secondary circuits could be attached as shown, or could be separated with

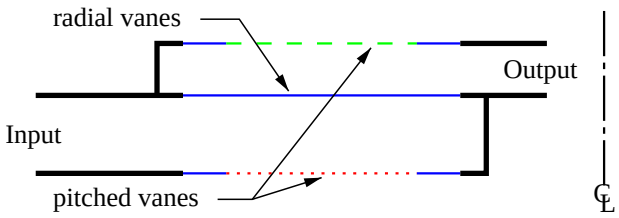

Figure 1. Simple transformer in cylindrical coordinates.

separate radial vane sections, or could consist entirely of pitched conducting sections.

A somewhat more complicated system (see Fig. 3) would use an auto-transformer, in which a portion of the primary and secondary circuits are shared. By using an auto-transformer design, the wrap angle of the primary coils can be reduced (for the same current multiplication) which makes the coils more robust. Moreover, the primary and secondary coils are closer together which increases the coupling efficiency, $\eta = M^2 / L_p L_s$, where L_p and L_s are the self inductances of the primary and secondary coils, respectively, and M is the mutual inductance between them. Since azimuthal current due to the driver should run in the same azimuthal direction in the primary and secondary coils, whereas the radial currents in these coils run in opposite directions, the wrap of these two coils must be in the opposite direction.

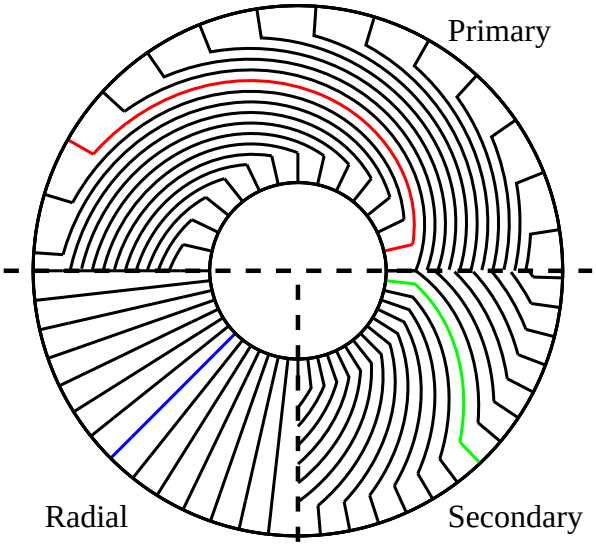

Figure 2. Composite r-θ view of transformer coils.

Fig. 4 shows a double-sided auto-transformer. This design reduces the wrap angle of any individual coil, and increases the coupling efficiency. To insure that the azimuthal current in all four coils flows in the same direction, the sign of the wrap angles should alternate for each of the stacked coils.

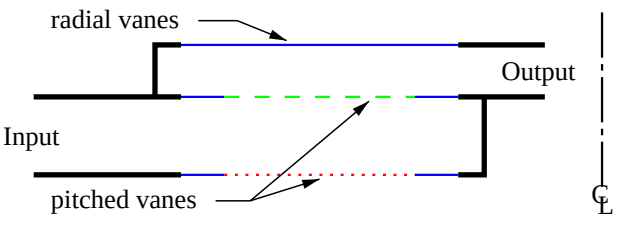

Figure 3. Auto-transformer in cylindrical coordinates.

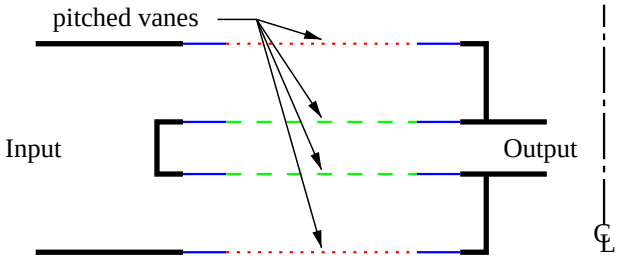

Figure 4. Double-sided auto-transformer in cylindrical coordinates.

2.0 TRANSFORMER MODELING

2.1 Calculation of Self and Mutual Inductance

The total inductance of a coil like the one shown in Fig. 2, which carries radial as well as azimuthal current, is the sum of the inductance associated with its radial current and the inductance associated with its azimuthal current. The portion due to the radial current, L_r, can be calculated analytically by replacing the coil with a solid disk. This approximation will slightly underestimate L_r because of the effect of the discrete coil windings. A discussion of this effect can be found in Appendix A. It can be shown that for a given coil configuration, and any geometrically similar configuration, the coil's inductance due to azimuthal current, L_θ, can be expressed in terms of a normalized inductance $\mathcal{L}$, i.e., $L_\theta = \mathcal{L}\delta\Delta\theta^2$, where $\Delta\theta$ is the total angle subtended by the vanes of the coil and δ is a length scaling parameter for similar coils, i.e., coils that change in size (i.e., δ or $\Delta\theta$), but not in shape. A coil's configuration includes its location, pitch figure, and any surrounding flux-excluding structure, which all need to be scaled in proportion to δ. We have chosen to define δ as the difference between the inner and outer radii of the spiral sections of the coils, i.e., $\delta = b - a$.

The pitch figure of the coil, i.e., the variation of the current pitch along the radial extent, can vary with radius and is defined to be $f(\rho)$, where $\rho = r/\delta$ and $\int_{a/\delta}^{b/\delta} f(\rho)d\rho = 1$. The coil's pitch is $P(r) \equiv r(d\theta/dr) = \Delta\theta\rho f(\rho)$. Note that two coils are geometrically similar only if their figures are the same. We have initially chosen to limit ourselves to $f = 1$. This choice of figure spreads the magnetic pressures on the coils uniformly while storing much of the magnetic energy near the load. Further, we will limit ourselves to transformer systems whose coils all have the same values of a and b.

Applying a similar process for two coils, p and s, in close proximity (see Fig. 5), and with the same δ, their mutual inductance M can be expressed in terms of a normalized mutual inductance $\mathcal{M}$, i.e., $M = \mathcal{M}\delta\Delta\theta_p\Delta\theta_s$. The coupling efficiency between the coils is then $\eta = \mathcal{M}^2/\mathcal{L}^2$ and depends only upon the shape of the entire device, but not the scale size as expressed by δ, $\Delta\theta_p$, and $\Delta\theta_s$.

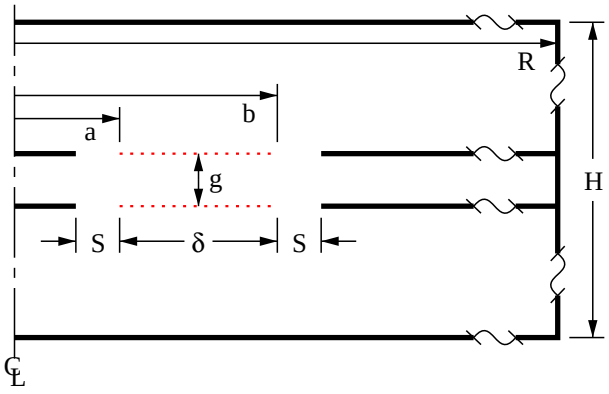

Figure 5. Geometry for Atheta inductance calculations. Note that *R* and *H* are not shown to scale.

The static magnetic code Atheta[4] was used to obtain values for $\mathcal{L}$ and $\mathcal{M}$. The geometry of the calculation is shown in Fig. 5. Atheta computes the vector potential **A** for coils whose windings carry current only in the azimuthal direction. Since **A** has only an azimuthal component, the resulting magnetic field (**B**) has only r and z components. To model our coil's azimuthal current we insert a large number of windings

(we typically have used 40-80) in the plane of the coil, choosing their spacing and/or current amplitudes to reflect the distribution of the coil's pitch figure, *f*. For the case of $f = 1$, we simply use equally spaced windings with equal current in each. If the azimuthal extent of each coil winding were the entire circumference of the coil ($\Delta\theta = 2\pi$), the total azimuthal current of the coil through any constant θ surface would equal the current driving the coil. Consequently, if the sum of the currents in all the Atheta windings is set to $1/2\pi$, then the inductance obtained from the simulation will be normalized relative to $\Delta\theta$ in radians. Similarly, if for any given coil aspect ratio (*b*/*a*), the dimensions of the coil are adjusted so that $b - a = 1\text{cm}$, then the simulation inductance will be normalized relative to δ in cm.

The Atheta calculations were done in a large bounding box (large *R* and *H*) so that the values calculated can be considered to be for free-space coils. Since the geometry shown in Fig. 5 is symmetric about the horizontal (z) plane midway between the two coils (shown in red), we only need to model the portion of the geometry above the symmetry plane. Using $B_z = 0$ as a boundary condition on the symmetry plane (equivalent to a perfect conductor), it can be shown that the inductance obtained for this half-geometry is $\mathcal{L}$-$\mathcal{M}$. Alternately, using $B_r = 0$ (a mirror symmetry boundary) yields the net normalized inductance $\mathcal{M}$+$\mathcal{L}$. From these two simulated inductances, the values of $\mathcal{L}$ and $\mathcal{M}$ can be obtained. Fig. 6 shows the coupling efficiency η for several values of *b*/*a* (see Fig. 5) as a function of the normalized gap g/δ.

In a realizable system, the coils will connect to short sections of radial conductors, which will in turn connect to solid conductors which are needed to provide their support. The latter will exclude flux, and will reduce both inductance and mutual inductance. This is shown in Fig. 5 where a standoff distance, denoted *S*, separates the coils and their flux-excluding support structure. Fig. 7 shows the normalized self and mutual inductances as a function of *S* for the case where $b/a = 2$ and $g/\delta = 0.075$. Also shown is the corresponding coupling efficiency. Note that the efficiencies shown in Fig. 6 are "ideal" in the sense that they were computed without any supports.

Because of the symmetry of the problem, and to the extent that $H >> \delta$, the self inductance $\mathcal{L}$ in the absence of flux-excluding structure should be independent of *g*. In fact, the variations in $\mathcal{L}$ observed are less than 0.1 percent. The introduction of the flux-excluding supports breaks the symmetry, and introduces a slight dependence of $\mathcal{L}$ on *g*. For values of $g/\delta < 0.15$ and $S/\delta > 0.2$, this

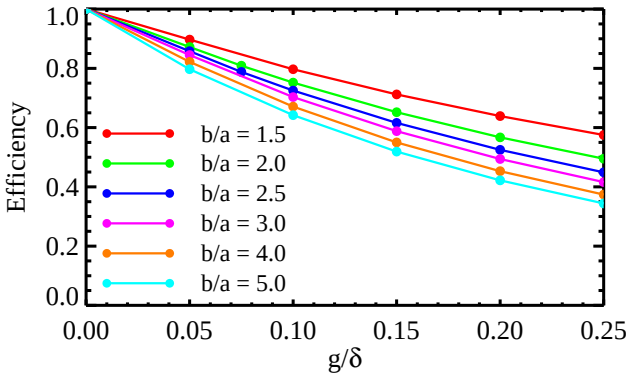

Figure 6. Transformer efficiency as a function of g for several ratios of outer to inner radius.

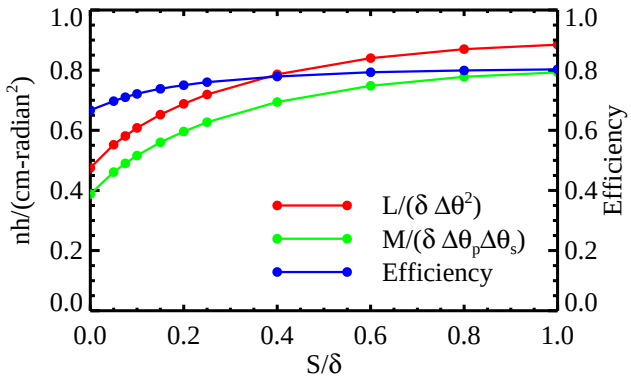

Figure 7. $\mathcal{L}$, $\mathcal{M}$, and η as a function of coil standoff *S* for $b/a = 2.0$ and $g/\delta = 0.075$.

variation no larger than ~3 percent. It is also observed that $\mathcal{M}$ decreases almost linearly as g/δ increases. Deviations in this behavior are bounded by ~4 percent for $g/\delta < 0.15$ and $S/\delta > 0.2$. Consequently, we can approximate $\mathcal{L}$ by its value at $g/\delta = 0$, which we will denote $\mathcal{L}_0$, and approximate $\mathcal{M}$ by $\mathcal{M} \cong \mathcal{L}_0 - \kappa(g/\delta)$, where κ is the observed slope of $\mathcal{M}$ with g/δ. Tables for $\mathcal{L}_0$ and κ for various combinations of b/a and S/δ can be found in Appendix B, along with an analytical derivation of κ. If a more accurate approximation for $\mathcal{M}$ is required, a quadratic coefficient κ_2 can be added, where $\mathcal{M} \cong \mathcal{L}_0 - \kappa(g/\delta) + \kappa_2 (g/\delta)^2$. With the quadratic term, this approximation is accurate to better than one percent for $g/\delta < 0.25$ and $S/\delta > 0.2$. Appendix B also provides a table for κ_2.

These data were encouraging, as the coupling efficiency and the inductances appeared to be reasonable for the devices we had in mind. While studying these data the idea of a double-sided auto-transformer occurred to us. The double-sided design (Fig. 4) has several advantages over the single-sided design of Fig. 3. Since the coil wrap angles need to be about half that of a single-sided design for the same inductance, the coils are stronger, or alternately, the inductance can be increased without increasing the wrap angle. Moreover, the coupling efficiencies are higher.

Atheta was used to compute $\mathcal{L}$ and $\mathcal{M}$ for a double-sided transformer, using the geometry shown in Fig. 8. Note that here we define $\Delta\theta_p$ and $\Delta\theta_s$ to be the wrap angle for single primary and secondary coils, respectively. Fig. 9 shows the coupling efficiency versus the normalized primary gap, g_p/δ, between the primary and secondary coils. Here we have used $b/a = 2.0$ and $S/\delta = 0.25$, which are values that appear to be reasonable for an actual transformer system. Efficiencies for three ratios of primary to secondary gap are shown, although the efficiency is relatively insensitive to this ratio. The efficiency for the corresponding single-sided transformer is also shown for reference.

The improvement of efficiency of the double-sided design over the single-sided design is appreciable, particularly for values of $g_p/\delta > 0.05$, which is a reasonable lower limit for the primary gap. Since the transformer is being used to increase the secondary current above the primary current,

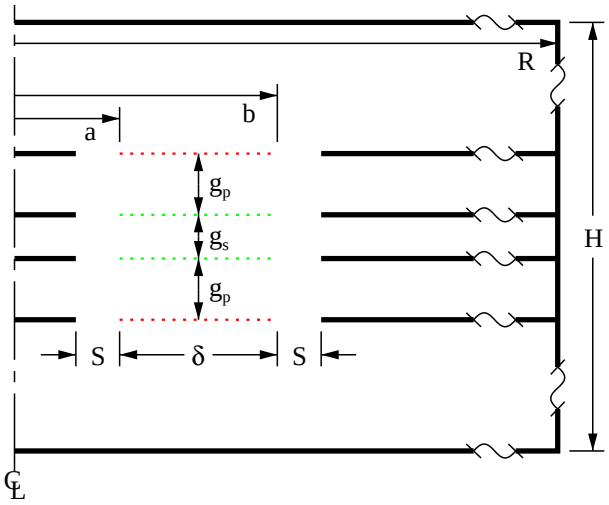

Figure 8. Geometry for Atheta inductance calculations of double-sided transformer.

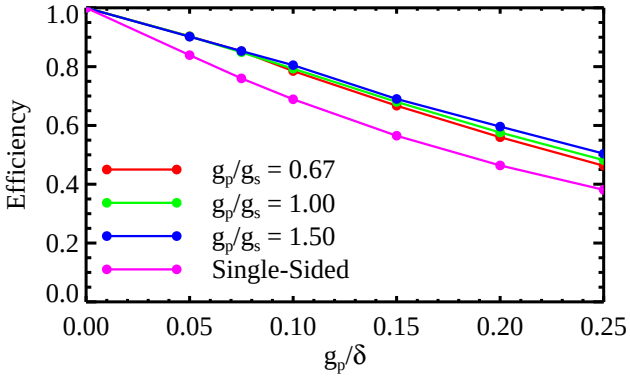

Figure 9. Double-sided transformer efficiency as a function of g_p for various ratios of primary to secondary gap. Single-sided efficiency is shown for comparison.

the voltages in the primary circuit will necessarily be greater than those in the secondary circuit. In this situation, it is likely to be desirable that g_p/g_s be greater than one. Even though the efficiency is relatively insensitive to this quantity, it does improve slightly as g_p/g_s becomes larger.

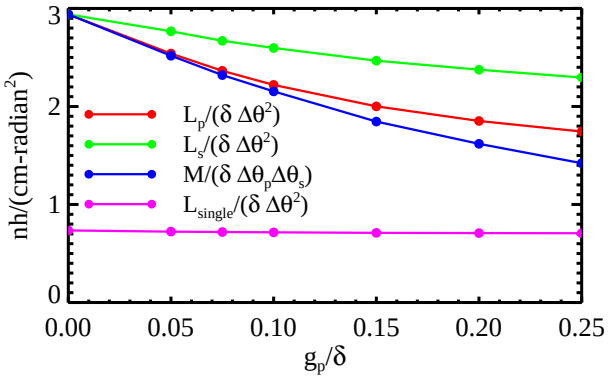

Figure 10. $\mathcal{L}_p$, $\mathcal{L}_s$, and $\mathcal{M}$ as a function of primary gap g_p. g_p/g_s = 1.5.

Fig. 10 shows the normalized primary, secondary, and mutual inductances for g_p/g_s = 1.5. Here again we have used b/a = 2.0 and S/δ = 0.25 as reasonable values for the coil's aspect ratio and support standoff distance. As all of the the gaps go to zero, the double-sided transformer's primary, secondary, and mutual inductances should approach four times the self inductance of a single coil (shown at the bottom), as they do. This is because the wrap angle has effectively been doubled.

2.2 Circuit Models for Transformer Systems

In the previous section, we described the self and mutual inductive properties of simple coils and coil pairs based upon their physical configuration. The simplest way to model the performance of these coils in actual systems is with lumped circuit modeling, which we will consider in this section. A circuit model is used to describe the interaction of the various components of an electrical circuit; in our case we will use it to describe the interaction of the coils comprising a transformer with the driver, or generator, and a load. In our case, we will model the generator with a Thévenin equivalent circuit, including any inductance associated with the input to the transformer, and we will assume that the load can be described by a possibly time-dependent resistance and/or inductance.

2.2.1 Basic transformers with inductive loads

The simplest transformer system that we can model is for the basic transformer, as depicted in Fig. 1, with a purely inductive load. This inductance can be time dependent, but we will defer until later a more specific description of the load. A diagram for this circuit is shown in Fig. 11. It is convenient to look at the inductance as seen by the source. We will call this inductance L_{eff}, which can be shown to be

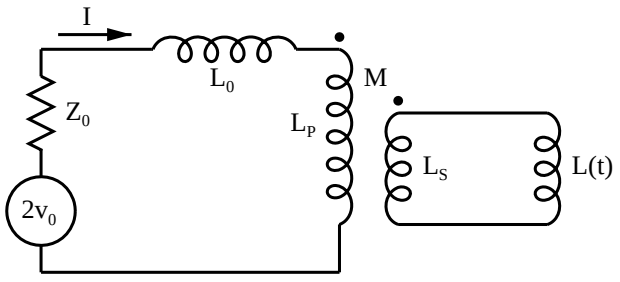

Figure 11. Circuit for basic transformer system.

$$L_{eff} = L_0 + L_p(1-\eta) + M^2 L(t)/L_s[L_s + L(t)],$$

where η is the transformer's coupling efficiency as defined in Section 1.1 above. A derivation of L_{eff} can be found in Appendix C. The defining circuit equation for the simple transformer is

$d(L_{eff}\,I)/dt = 2v_0(t) - Z_0 I$, where the forward-going voltage $v_0(t)$ and source impedance Z_0 describe the driver's Thévenin equivalent source.

2.2.2 Auto transformers with inductive loads

The auto transformer, as depicted in Fig. 3, although more complicated than a basic transformer, can still be modeled with an effective inductance for the case of a purely inductive load. Fig. 12 shows the diagram for the auto transformer's circuit. in this case, the effective inductance seen by the source (see Appendix C) is given by

$$L_{eff} = L_0 + L_p(1-\eta) + M^2 L(t)/L_s[L_s + L(t)]\,.$$

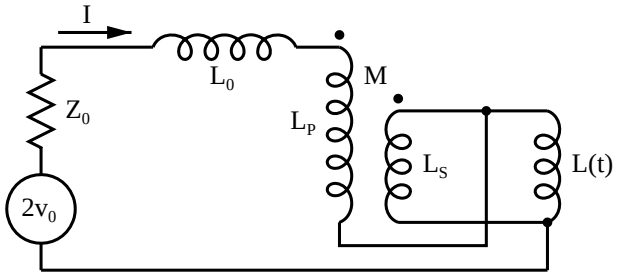

Figure 12. Circuit for auto transformer system.

Note that the double-sided auto transformer can be modeled using this same simple circuit. This is because of its symmetry (see Fig. 4). Values of L_p, L_s, and M can be obtained by using circuit model equations for the two loops in Fig. 4, which include the self and mutual inductances of all four coils. These can be algebraically manipulated into the form of (C6)-(C9), which correspond to the circuit shown in Fig. 12. Alternately, L_p, L_s, and M could be found by using the analysis described in Section 2.1 above, but applied to the geometry shown in Fig. 5.

2.2.3 Circuit models for plasma radiation source loads

Plasma radiation source (PRS), or z-pinch, loads convert the magnetic energy of the driver's current into kinetic energy of a cylindrical shell of material so that the material converges radially toward the shell's axis. The material stagnates on axis, converting the kinetic energy into heat and radiation. This type of load is important to model because it is probably the most stressful to the transmission and current addition components in high-current driver systems.

It is easy to show that for such systems the force that is exerted on the load's mass by the driver's magnetic field is $F = (I_{load}^2/2)\,dL_{load}/dr$, where I_{load} is the current delivered to the load, L_{load} the inductance of the load, which is time dependent, and r is the radial position of the shell, which we will assume is of infinitesimal thickness. Applying Newton's Second Law to the load's mass, using this force, yields a second-order differential equation for the radial position of the converging shell. This must be solved simultaneously with the defining circuit equations, which we have shown is a single first-order differential equation for a transformer system with a purely inductive load. Although this is a very good model of physical z-pinch, it clearly breaks down as r approaches zero, since F becomes infinite. In an actual z-pinch there are forces which rapidly decelerate the material near the axis. However, these forces are quite complex, and a circuit model based on the actual physical properties is not realistic.

A common approach to this problem is to simply choose some radius, typically ~10% of the original radius, at which to stop accelerating the shell.[5] Other approaches are based on using

idealized retarding forces that mimic the proper behavior as the shell approaches the axis. For example, if one assumes the shell is filled with an ideal gas with an initial pressure P_o, it will exert a radial outward force that will increase inversely with the square of r. The value of P_o is then chosen to best approximate the observed rate of the shell's convergence. The advantage of this model is that the load remains a simple inductor and that the number of differential equations that need to be solved remains the same. However, this force does not mimic the radial dependence of the real retarding forces well; in fact, there is clearly some small radially-outward force before the shell even starts moving.

A perhaps better approach, and one that we will use for the modeling described in this report, is to assume the shell is filled with a very low-density (i.e., its initial pressure is negligible) ideal gas that is ohmically heated with the load current. The resistance of the gas is chosen to best mimic the behavior of actual z-pinches as they approach stagnation. With this model, a series resistance is added to the load circuit. With this addition, we can no longer model the circuit with a single first-order equation and an effective inductance; but require two first-order equations whose variables are the source and load currents. An additional first-order equation is required to model the internal energy of the gas as it is heated and compressed. The details of this model, as well as the simpler model described in the preceding paragraph, are described more fully in Appendix C.

2.2.4 Circuit model for a convolute driver system

Since the primary purpose for investigating transform-based systems for high-current drivers is to determine the advantages of such a system to a conventional convolute-based system, it is desirable to have a circuit model for a convolute driver in order to compare the potential performance of the two approaches. We will use a model based on one developed by Struve[5] which has been used to analyze PRS data from Z. A diagram of the circuit is shown in Fig. 13. We've made two changes in the model. First, we use the PRS load model described above as opposed to the minimum radius approach that he used. Struve used a constant $Z_{loss} = V_1/(I_o^2 - I^2)^{1/2}$ model, where Z_{loss} was set below the electron loss value to compensate for closure at the nulls due to material from the anode. We are using a time dependent Z_{loss}, whose intial value is the electron-loss-only value calculated by Pointon[6] for the Z convolute (0.4 Ω). When the energy deposition in the anode at the convolute reached an assigned threshold, we let the value of Z_{loss} decay exponentially with an assigned time constant. The threshold (25 kJ) and the time constant (50 ns) were set using data from isentropic compression experiments studied by Lemke.[7] These data had more accurate downstream current data than have been available in the more severe conditions near a Z pinch.

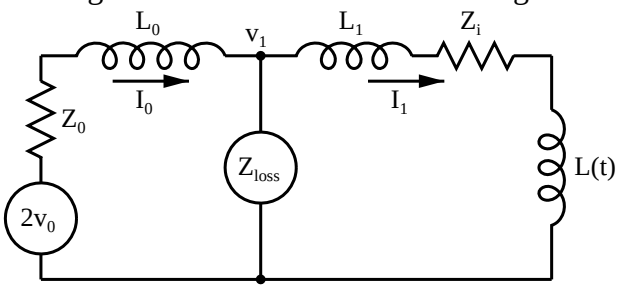

Figure 13. Circuit for a convolute driver system.

2.2.5 *Auto-transformer/convolute comparisons for a Z-like driver*

The Thévenin-equivalent source for each of Z's four parallel drive lines is 3 MV at 0.48Ω. For an equivalently driven auto transformer system, we will assume a four-level system added in series rather than in parallel. The Thévenin-equivalent source for this equivalent series source is defined by v_0= 4×3.0 = 12 MV, and Z_0 = 4×0.48 = 1.92Ω. Because of the characteristics of magnetically insulated flow, and also because desorbed gas and plasma closure rates tend to be independent of voltage, the impedance of the single MITL can be much lower than four times that of the present Z MITLs. However, the inductance near the insulator stack will be something like four times that of one of the Z levels. Our best estimate for L_0 is 50 nH.

Using the Atheta data, reasonable transformer parameters were chosen to be (see Fig. 8): a=20 cm, b=40 cm, g_p=1.5 cm, g_s=1.0 cm, $\Delta\theta_p$=2.4 radians (×2), $\Delta\theta_s$=0.7 radians (×2). From this, and including inductance from B_θ, L_p = 331 nH, L_s = 28 nH, M = 84 nH, η = 0.76 (see Fig. 12). This adds the constant amount $(L_1\text{-}M^2/L_2) = L_1(1\text{-}\eta)$ = 79 nH to L_0.

For our comparison, we will choose parameters for the PRS load model that were optimized for coupling to the Z convolute-based system. The initial radius of the shell is 1.5 cm, its axial height is 2 cm, and its total mass is 5.46 mg. The radius of the load's outer conductor is 2.0 cm, which gives an initial load inductance of 1.15 nH. The small (~3 mΩ) series resistance that is used to heat the low density gas in our load model, Z_i, was chosen so that the maximum internal energy in the gas load, and also the minimum radius, occur at the time of the X-ray peak for the appropriate Z experimental shot. This same load is also used in the auto-transformer model. The circuit for this model is same as the circuit shown in Fig 12, except for the addition of Z_i in series with the load inductance $L(t)$. Because of this addition, L_{eff} is no longer strictly valid, since the circuit equation now requires two coupled equations. However, because Z_i is so small, general characteristics derived from L_{eff} are reasonably accurate.

The differential equations for the auto transformer coupled with the low-pressure, heated gas PRS model can be converted to difference equations for numerical solution. This is described in detail in Appendix C. Difference equations for the convolute model depicted in Fig. 13, coupled with the same load model, were also developed. Procedures to solve these systems of difference equations were implemented using the commercial IDL* software, complemented by the PFIDL data analysis tools.[8] Results from these solutions can be compared to evaluate the potential relative performance of a transformer system on a Z-like driver to Z's current convolute system. Fig. 14 shows the time-dependent load currents and the internal energy of the load for both systems. Although the internal energy of the

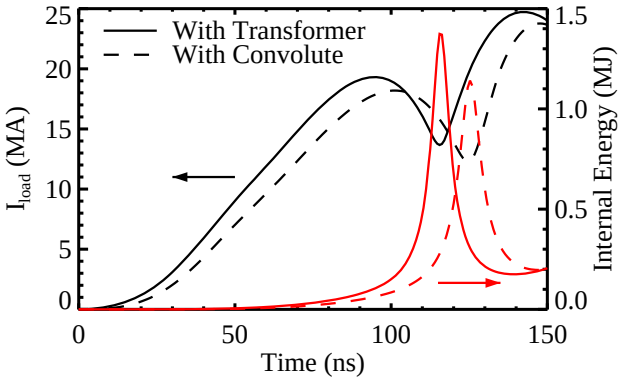

Figure 14. Comparison of load current and internal energy between transformer and convolute systems.

* IDL is a product of ITT Visual Information Solutions, http://www.ittvis.com.

load model's low-density gas is not strictly a measure of the energy available for conversion to radiation in an actual device, it provides a reasonable approximation for that quantity and its comparison for the two systems is indicative of the relative performance of the two systems.

There are some caveats associated with this comparison that should be noted:

- No attempt to optimize the transformer model's parameters was made,
- The parameters for the PRS load have not been re-optimized for the transformer,
- There are no electron losses in the transformer model at present.

The first two items presumably cause the transformer modeling to under-perform its potential, but the third definitely neglects losses that will occur, consequently over-estimating its potential. Although one or more Z_{loss} components are likely to be suitable, we will defer that question for now, and rely on results of electromagnetic Particle-In-Cell (PIC) simulations to provide detailed knowledge of the behavior of electrons in a transformer system.

2.3 Electromagnetic Modeling

The transformer coils are three-dimensional objects as they are only invariant to rotations of multiples of $2\pi/N$ where N is the number of vanes in the coil. However, if N is very high (we expect to use 40 and 100 vane coils) these coils can be modeled as two-dimensional objects, as if N were infinite. There is additional inductance due to the finite number of vanes, which is discussed in Appendix A, but it is small, and neglecting it is acceptable.

Although there is a coordinate system for which the individual coil vanes conform to coordinate lines, we do not have tools using coordinate systems other than Cartesian, cylindrical, or spherical coordinates. However, the 2D/3D electromagnetic, particle-in-cell simulation code Quicksilver[2] can model coils with an infinite number of vanes by using a tensor conductivity model in the plane of the coils. A description of this model can be found in Appendix D.

Although the primary goal of using Quicksilver to model transformer systems is to evaluate their operation in the presence of electron flow, it is useful to use it in its fields-only mode to model a system with the same transformer parameters as were used for the Z-like transformer-based driver that was described in Section 2.2.5 above. It is easy to show that the values L_p, L_s, and M can be determined from measurements from two simulations, one with an open-circuit load in the secondary, and one with a short-circuit load. Figures 15 and 16 show contours of the magnetic stream function in the r,z plane for the short-circuit and open-circuit simulations, respectively.

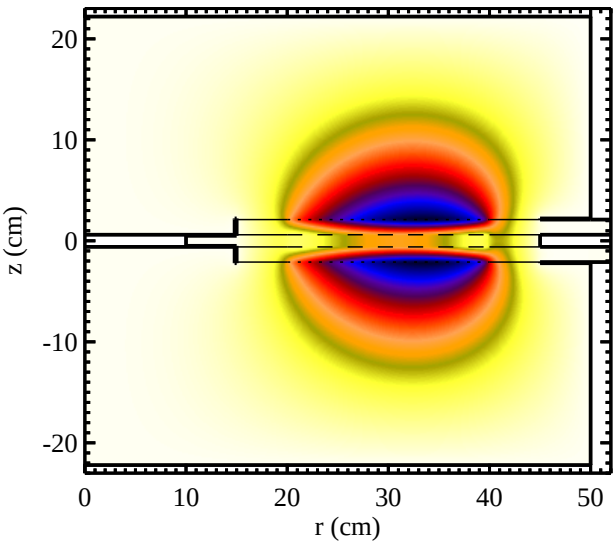

Figure 15. Stream function from Quicksilver simulation of a double-sided transformer with a short-circuit load located at r = 10 cm.

For the short-circuit load, we can measure the current amplification ratio $R_{sc} \equiv I_s / I_p$. Then for both cases, measured input voltages can be integrated over time to obtain the flux in the circuit, which can be divided by the input current to obtain the effective inductance of the circuit. If we denote those two measured inductances as L_{oc} and L_{sc}, respectively, it is easy to show that

$$L_p = L_{oc} - L_0 - L_{ld} + \frac{(L_{oc} - L_{sc})(2R_{sc} - 1)}{R_{sc}^2}$$

$$L_s = \frac{L_{oc} - L_{sc}}{R_{sc}^2} - L_{ld}$$

$$M = \frac{(L_{oc} - L_{sc})(R_{sc} - 1)}{R_{sc}^2} - L_{ld}$$

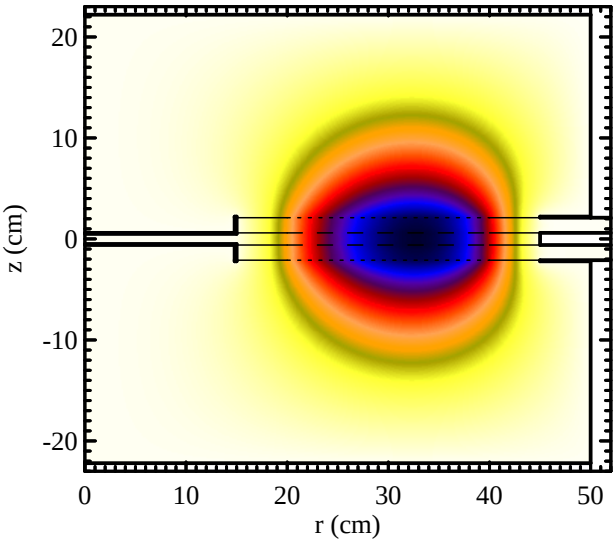

Figure 16. Stream function from Quicksilver simulation of a double-sided transformer with an open-circuit load.

where L_0 and L_{ld} represent, respectively, the inductances associated with azimuthal magnetic fields in the primary and secondary circuits. Note that these two values are easily calculated from the geometry of the system. The interested reader is referred to (C9) in Appendix C, which can be manipulated to obtain these equations. Comparing the values obtained from these equations using the measurements from the two Quicksilver simulations, we find that they agree to within about 1% with values computed from Atheta using the geometry shown in Fig. 8 with the same physical dimensions as the Quicksilver simulation.

We can also run a fields-only simulation of the same transformer geometry with a PRS load. A model for this load, equivalent to the circuit model described in Section C.3.3 below, has been implemented in Quicksilver.[7] For this case we use the same parameters for the PRS load that were used in the comparison described in 2.2.5 above. Fig. 17 shows the time-dependent load currents and the internal energy of the load for this system as predicted by the circuit model and by 2D EM simulation. Not surprisingly, the agreement is quite good.

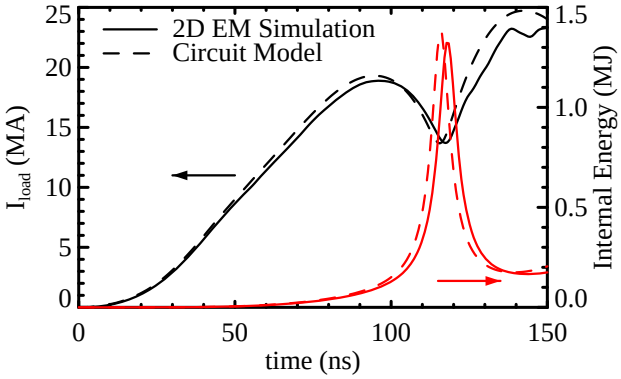

Figure 17. Comparison of 2D EM simulation with circuit model for Z-like transformer system.

2.3.1 Particle-in-Cell Modeling of Electron Flow

In addition to the simulation of electromagnetic fields, Quicksilver also can self-consistently treat the motion of charged particles[4] using the Particle-in-Cell (PIC) method. These particles are

accelerated by the time-varying electric and magnetic fields, and their resulting motion provides current that is a source for the EM fields. We will use that capability to model the effect of electron flow on transformer systems. In particular, we will begin by simulating the Z-like transformer system that was modeled electromagnetically in the previous section, but allowing the emission of electrons from the surfaces of negatively-charged electrodes (cathodes) of the system. Note that this also includes the surfaces of the coils. As a part of the implementation of the 2D coil model in Quicksilver, models for the emission of electrons from coil surfaces, as well as models for any other interaction between the coils and electrons, needed to be developed. The interested reader is referred to Section D.2 in Appendix D for the details of these models.

While electron currents flow in these high-voltage systems due to space-charge-limited emission from cathode surfaces, the losses due to these currents are often limited. This occurs because the flows are inside transmission lines that are made of highly conductive solid surfaces, so that electromagnetic forces are normal to these surfaces. The electrons can only transfer axial momentum to the electrodes through colliding with them, and since their momentum flux is limited by their energy, mass, and current, the electromagnetic pressure difference between upstream and downstream of a loss is limited, and therefore the current is limited.

In the systems with convoluted current adders, the electron losses are largely determined upstream of the convolute,[1] and by themselves would not constitute a serious loss.[6] However, these losses are concentrated in very small areas at magnetic nulls, producing high anode temperatures[9,10] and large gas loads that undergo breakdown and generate arcs.

In our transformers, on the other hand, the coils are not solid surfaces, but have an azimuthal component that exerts a radial force on the magnetic field, which in turn exerts a radial force on the electrons. These fields are very strong, being much larger than the azimuthal fields at the outer periphery of the coils, and can cause heavy electron losses.

In simulating our transformer systems, there are two distinct types of surfaces upon which electrons can be collected: solid surfaces, where every electron crossing the surface is captured; and coil surfaces, where electrons may be captured, or may pass through. Simulations were run with capture probabilities from 0 to 1.0. When the probability was zero, the simulations were very noisy, but probabilities between 0.1 and 1.0 had little effect on currents and other macroscopic quantities in the simulation. For probabilities less than 1.0, electrons can access the regions behind the electrodes, as one would expect. In the simulation results that follow, we use a capture probability of 0.5 for electrons striking the coil surfaces.

Using the set of coils for the transformer shown in Figs. 15 and 16, we found that the losses were much too large to be acceptable. Figure 18 shows a view of the conductors and coils with the correct *r*-*z* aspect ratio. Figure 19 shows, for both the upper and lower primaries, the currents just outside the transformer (see Fig. 18) and the currents in the middle of the primary coils. It also shows

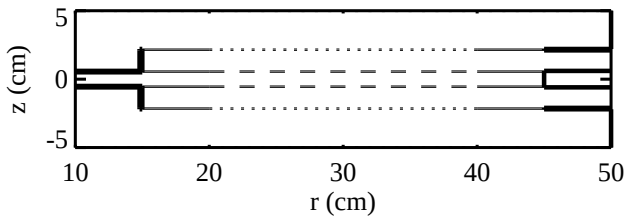

Figure 18. *r-z* cross-section of Z-like transformer with 1.5 and 1.0 cm primary and secondary gaps, respectively.

the secondary or load current. The peak value of the load current is 13.5 MA, well below the 18.2 MA in our convolute circuit model (see Fig. 14), and the 18.9 MA for the transformer system 2D simulation with no electron loss (see Fig. 17). As a result, the peak internal energy reaches only 0.552 MJ compared to 1.14 MJ for the convolute system and 1.33 MJ for the lossless transformer.

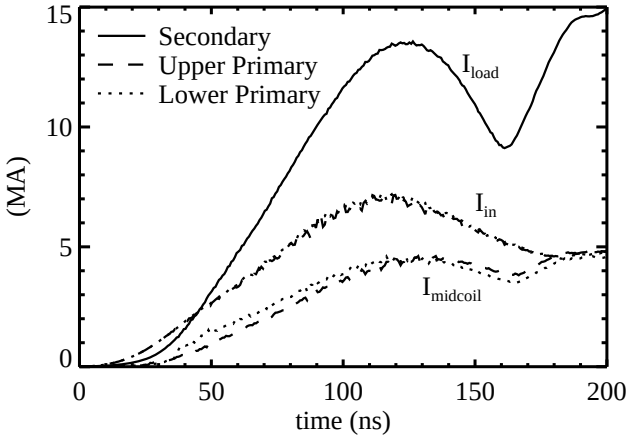

Figure 19. Simulation currents for transformer system shown in Fig. 18.

Figure 20 shows the electron density throughout the transformer. Notice the difference between the upper and the lower primary sections. In the lower section most of the region between the primary and secondary coils has appreciable electron density because the coil is emitting electrons, which must travel along field lines. At this time (108 ns), the load impedance is still low (see Fig. 19), and most field lines do not yet penetrate the secondary coils, similar to Fig. 15. In the upper section, the secondary coil is emitting the electrons which then follow field lines to either end of the primary coil. Much of the region between the upper primary and secondary is virtually empty of electrons. Because the electrons in the region centered between the inner and outer coil radii drift largely in the $\mathbf{E}\times\mathbf{B}$ direction (i.e. roughly along the primary field windings), the electron current path generally parallels the primary windings, and in the bottom section can actually improve the coupling because the flow is closer to the secondary coil, effectively reducing the gap between the primary and secondary coils.

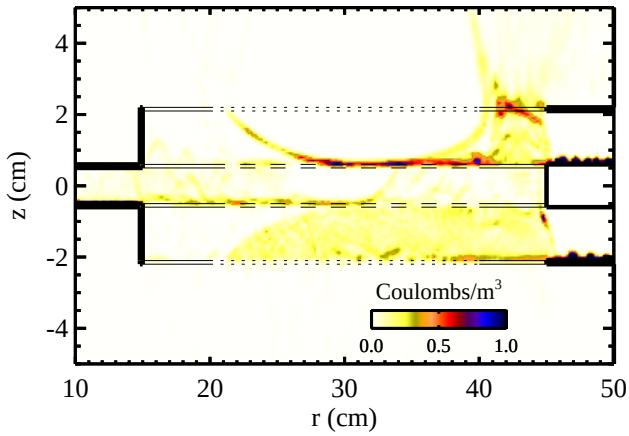

Figure 20. Simulation charge density at 108 ns for transformer system shown in Fig. 18.

Figure 21a shows the enclosed current ($2\pi r B_\theta/\mu_0$) throughout the transformer. Fig. 21b shows the enclosed current as a function of r at two axial locations, indicated by the two red horizontal dotted lines shown in Fig. 21a, close to the primary coils. Notice that there is appreciable recapture of current back to the coil near the inner radius of the bottom section. Also notice that the lost current is generally outside the coil outer radius in both top and bottom sections.

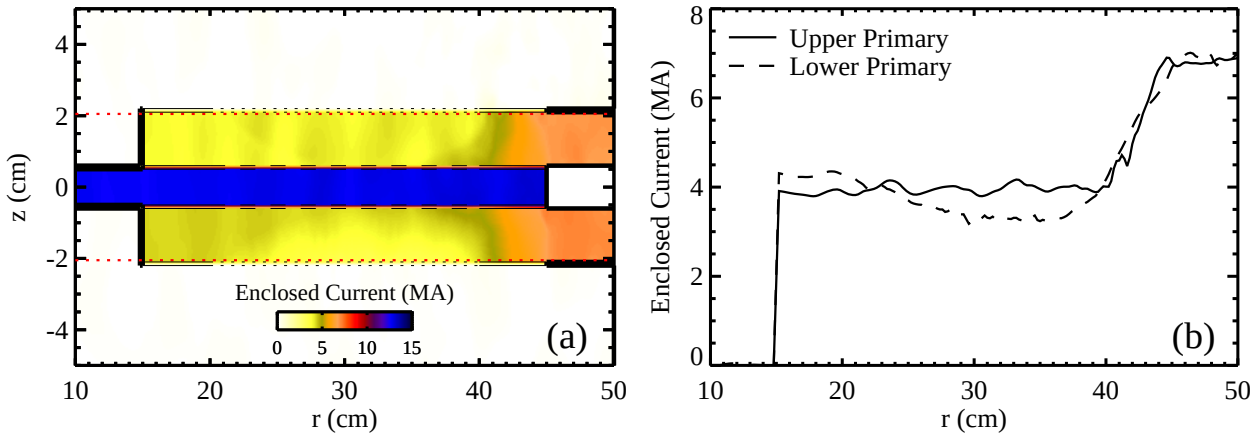

Figure 21. Simulation enclosed current for transformer system shown in Fig. 18. (b) shows radial variation at two axial locations, indicated by red horizontal dotted lines in (a).

No effort was made to optimize the coil windings or the PRS load parameters for this case, because we wanted to first attempt to reduce the electron losses at the outer radii. The losses are occurring along field lines which are generally in the *z* direction, as can be seen from the plot of the magnetic stream function in Fig. 22. If we can extend the length of these paths, the *z* component of the electric field, and therefore the charge, will be reduced (recall that the *z* component of electric field is zero at the cathode). Also, by the same path extension the lifetime of the electrons will be increased since the voltage is unchanged, so the mean their mean velocity is unchanged while their paths are longer. If we can extend the path the electrons between the electrodes, we can increase their lifetime and decrease the amount of charge in the region, thereby decreasing the loss current by the square of the ratio of the two path lengths.

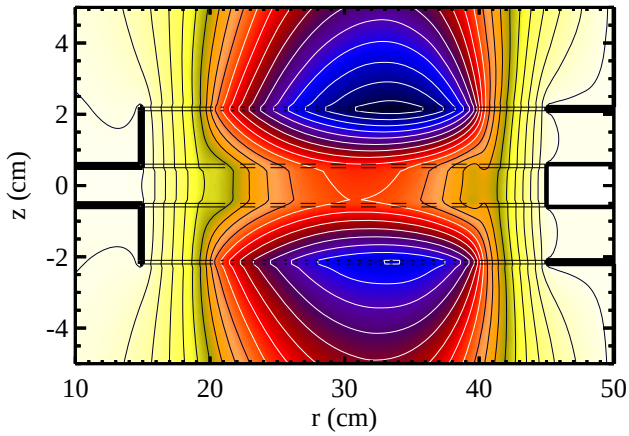

Figure 22. Simulated magnetic stream function at 108 ns for transformer system shown in Fig. 18 showing magnetic field lines.

To accomplish this we increased the gap between the outer current feeds from 1.5 cm to 3.0 cm, as shown in Fig. 23. This change included both the solid electrodes for $r > 45$ cm and the radial vanes between 40 and 45 cm radius. The inner ends of the radial vanes were then connected to the outer ends of the spiral coil vanes via axial vanes at $r = 40$ cm. The gaps between the primary and secondary coils were not changed, so the coupling efficiency was nominally unchanged. Increasing the gaps did indeed have the desired effect, as can be seen in the current plots in Fig 24. This brought the peak load current to 14.9 MA and the peak

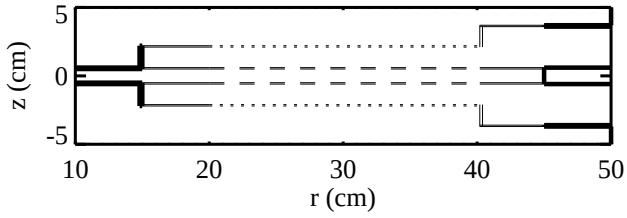

Figure 23. *r-z* cross-section of Z-like transformer with 1.5 and 1.0 cm primary and secondary gaps, respectively, and extended 3.0 cm feed gap.

internal energy up to 0.686 MJ, but still well below the values for the transformer system in the absence of electrons and for the convolute circuit model.

Encouraged by this result, the current feed gap was increased to 5 cm, as shown in Fig. 25. The currents from this simulation are shown in Fig. 26. The peak load current was 15.2 MA, and the peak internal energy was 0.725 MJ. Examining the enclosed current, as shown in Figs. 27a and 27b, it appears that the electron loss is taking place in a thin cylindrical region at the outer radius of the coil. The path of most of this current loss extends only about 1.5 cm between the secondary coils and the outer end of the primary coils.

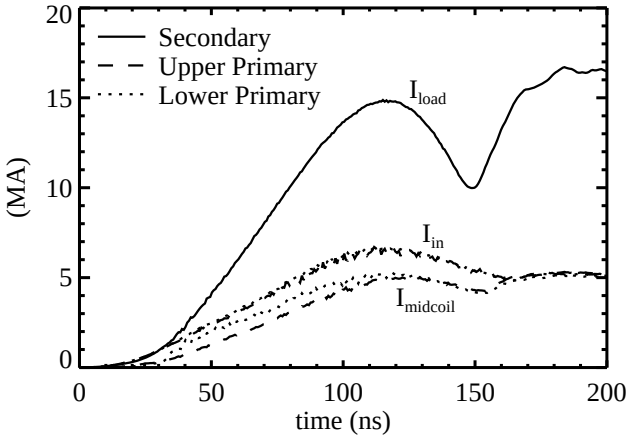

Figure 24. Simulation currents for transformer system shown in Fig. 23.

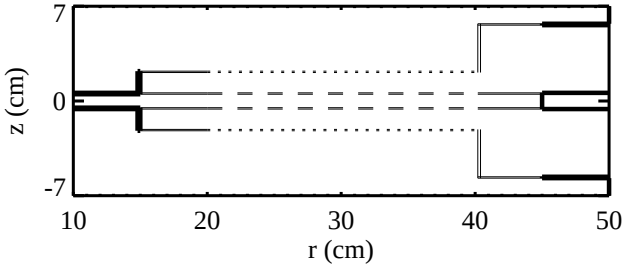

Figure 25. *r-z* cross-section of Z-like transformer with 1.5 and 1.0 cm primary and secondary gaps, respectively, and extended 5.0 cm feed gap.

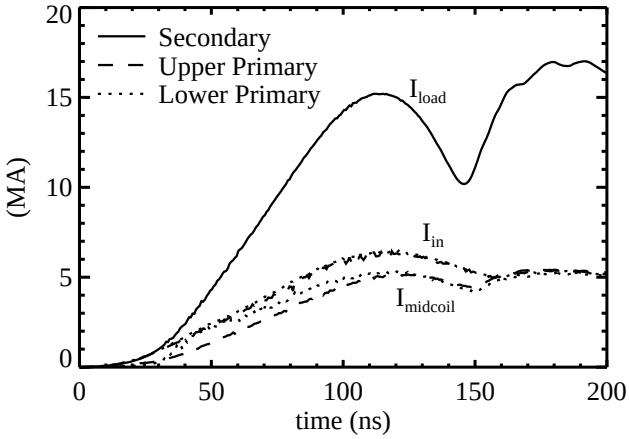

Figure 26. Simulation currents for transformer system shown in Fig. 25.

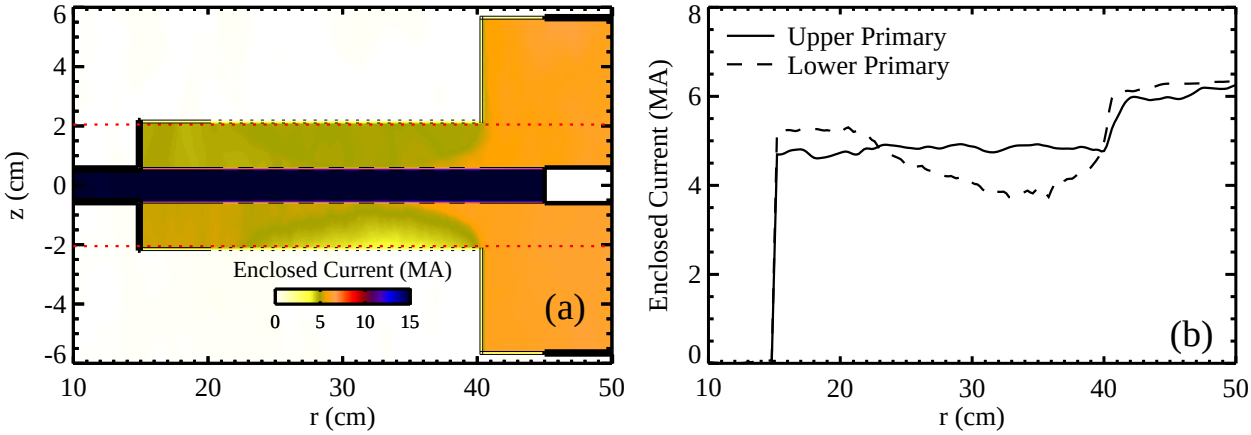

Figure 27. Simulation enclosed current for transformer system shown in Fig. 25. (b) shows radial variation at two axial locations, indicated by red horizontal dotted lines in (a).

From this, and from comparing the electrons losses for the three cases we described above (see Fig. 28), it appears that no appreciable further reduction can be gained by further increasing the gap. Nevertheless, we have achieved a 57% decrease in the electron loss by this modification. Fig. 28 also shows the electron loss current obtained from the convolute circuit model for comparison. Notice that the integrated charge for each of the three transformer systems is comparable to, if not less than, that of the convolute system. Figure 29 shows the internal energies achieved for these three cases. The internal energy was increased by 31% by expanding the primary feed gap to 5 cm, but the peak internal energy with the transformer is only 74% of that from the convolute model.

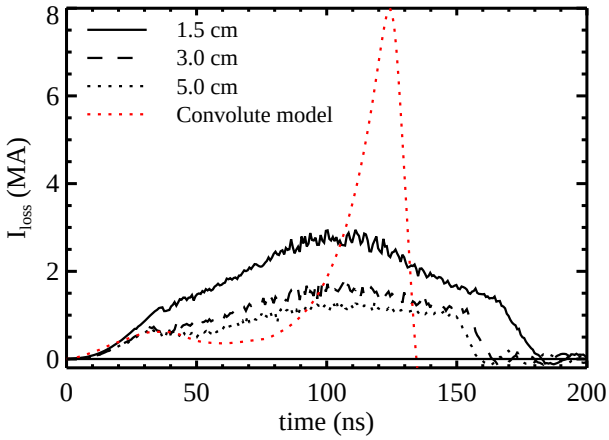

Figure 28. Comparison of electron loss current from 1.5, 3.0, and 5.0 feed gap simulations. For reference, the loss current from the convolute circuit model is shown in red.

We did not have adequate time to optimize either the transformer or the load for the transformer system. It is likely some appreciable performance improvements could be made by doing so, since the time of peak implosion is at about 150ns for the above data, whereas it was found that 120 to 130 ns was best for the convolute and loss-free transformer cases. The pulsed-power driver was the same in all cases.

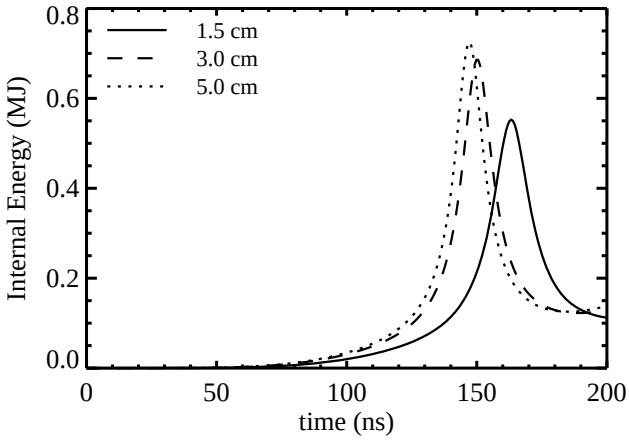

Figure 29. Comparison of PRS load internal energy from 1.5, 3.0, and 5.0 feed gap simulations.

In addition, there are other possible strategies for reducing electron losses. The shape of the field lines in the region near the outer radius of the primary coils might be improved by "shimming." This is similar to the method commonly used to improve the field uniformity near the end of a solenoidal magnetic field coil. A method applying this idea to our primary coils might be to increase the pitch of the field coils near the outer radius, and/or add some pitch to the presently axial vanes where they meet the primary coils. It might be possible to make a small improvement in coupling efficiency in the process. These are modifications that could be tested using the present capabilities of our simulation tools. Presently, our 2D coil model is restricted to coil sections that lie in constant surfaces of one of the three coordinates of the systems. However, it might be possible to make an improved coil design by using more arbitrary coil surface configurations. Significant enhancements to our existing simulation tools would be required to model such configurations.

Although electron loss is the root cause of all current loss in the convolutes used to add transmission lines in parallel,[6] the losses would be minor if the they consisted of electron current

alone. The major source of current loss, and one that eventually becomes a direct short, is due to arcs caused by gases driven from the anode by the electron loss.[7] The causal electron losses in the convolute occur at multiple magnetic nulls near each convolute post, but particularly at the null between neighboring posts. Efforts to mitigate the problem by lengthening the null have been somewhat successful, but there are limits to what can be done using this approach.

As we have discussed, there are appreciable electron losses in the transformers. Since the coils are invariant under axial rotations of $2\pi/N$, where the large number N is the number of vanes in the coil, the transformers are essentially two dimensional devices, and there can be no nulls if power is flowing radially. Because of the large circumference at which the power enters the transformer, the electron loss is actually greater than that of the convolute, at least for systems we have tested at this time. However, also because of the large circumference, the electron loss density is low due to the large area over which it occurs.

For the double auto-transformer system we have been analyzing in this section, the heating due to electron loss at the input of the transformer is small, and probably could be made even smaller by judicious improvements in primary coil design in the input region. There is more heating inside the transformer where much of the electron current that is flowing radially inward (as well as azimuthally) is recollected at the inner end of the primary coil.

Fig. 30a shows the heating of the electrodes projected by the simulation for the 5 cm feed gap design, calculated by considering energy and angle of impact for all electrons as they strike the coil surface.[11] Because the simulated coils are uniform surfaces, and many electrons are collected at near-grazing angles, these temperature predictions are probably somewhat higher than they would be for a real coil with discrete vanes. Figure 30b shows the enclosed current at four axial locations indicated in Fig. 30a by the four dotted red horizontal lines. The slopes of the enclosed current profiles are the z-directed current per radial length. This can only consist of electrons; consequently, a negative slope indicates electrons moving in the positive z direction.

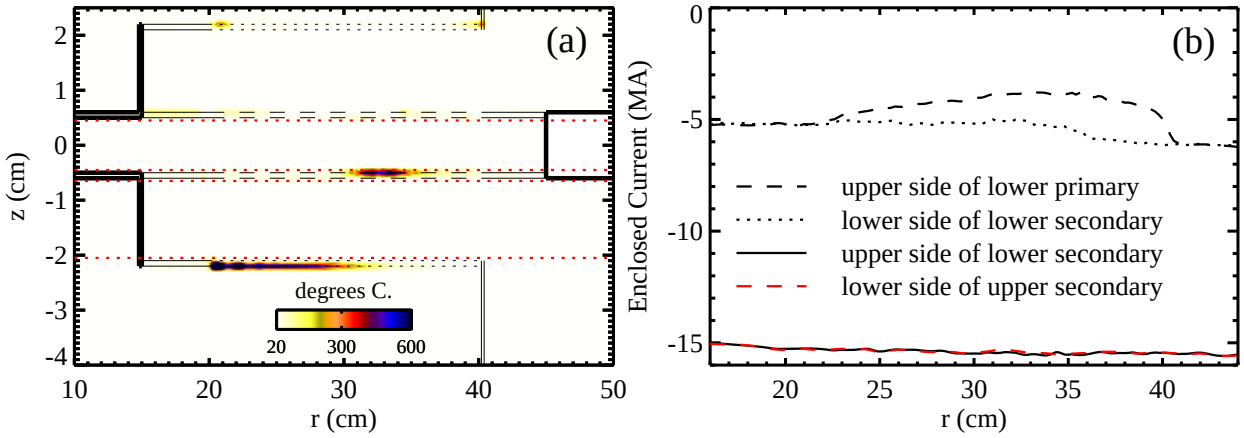

Figure 30. (a) Simulation electrode temperatures due to electron heating for the transformer system shown in Fig. 25. (b) shows the radial variation of the enclosed current at four axial locations, indicated by the red horizontal dotted lines in (a).

The heating of the lower primary coil by the flow current being returned at its inner end is by far the largest, increasing the temperature to 1700°C (it was initially 20°C), but this is a region where loss current should not be a problem because the axial electric field is very small. The heating of the outer radius of the lower secondary coil is more problematic since the axial electric field here is significantly larger, but the temperature increase is much lower (to ~500°C), and would be even lower if the current loss in the region were reduced. The heating due to current loss in the secondary is found to be minimal.

2.4 Analysis of Magnetic Forces on Transformer Coils

Both during and after the power pulse, the high magnetic fields in the transformer exert force on the transformer coils, which if large enough can cause mechanical damage. There are two possible damage mechanisms that need to be considered. The first is due to the magnetic pressure pushing transformer coils apart between the start of the power pulse and the time of maximum implosion. Fig. 15 shows the configuration of the field during this phase. The second is due to magnetic pressure after this time, including the time after the pulse when residual currents remain in the system. These currents can remain large for a considerable length of time if the vacuum insulator flashes, trapping flux in the system. During this later phase the magnetic field's configuration is like that shown in Fig. 16, and the forces tend to squeeze the coil vanes together midway between their inner and outer radii. This has been seen previously in experiments with fast field coils made with very thin vanes.

The force that a magnetic field exerts on an inductor is given by $F = (I^2/2)(dL/ds)$, where I is the current in the inductor and dL/ds is the change in inductance per distance the coil has deflected. Clearly during the power pulse, this deflection is small, since the coil outweighs the wire load by orders of magnitude, and the load only moves centimeters. Nevertheless there is energy deposited in the coil, which we will now calculate as follows. By integrating the force over time, we can obtain the total impulse P imparted to the coils. The energy deposited is then $P^2/(2M_c)$, where M_c is the mass of the coil. Although dL/ds is time dependent, we will use a time-independent upper bound for its value, so that the only time dependence to the force is though the current I. Defining ψ to be the integral of the square of the driving current, the impulse is then $P = (dL/ds)\psi/2$.

In the early-time phase, the force is axial; consequently $s = z$ in this case. As can be seen from (C4) and (C9), the only z dependence of the effective inductance of a transformer (or auto-transformer) system is through the mutual inductance M. Since M decreases as the separation between coils increases, it is easy to show that approximating the effective inductance by $L_p - M^2/L_s$ will provide an upper bound for dL/ds. If (B12), with only the linear term, is used to approximate M, it can be shown that $dL/ds \cong 2\kappa(\Delta\theta_p)^2$. Values of κ are tabulated in Table B2 over a wide range of coil parameters. If we use the coil parameters for the Z-like transformer system described in Section 2.2.5, we find that $dL/ds \cong 80$ nH/cm . Using the primary current from the circuit simulation of the transformer described in that same section, we obtain $\psi \approx$ 1.5x10^6 ampere^2-seconds. This gives an impulse of ~6 Newton-seconds. Estimating the mass of

the spiral part of the two primary coils to be about two kilograms, we find the energy deposited is ~9 Joules, which is unlikely to be significant.

Treating the late-time forces is more complicated, but we will choose an approach that avoids some of the difficulties by sacrificing some accuracy. Even so, our estimate for energy deposited in the coil should be accurate to a factor of two, more or less. As stated earlier, the forces in this phase tend to squeeze the coil vanes toward a radius midway between their inner and outer radii. This tends to reduce the pitch of the coils near the two ends of the coil, and increase the pitch toward the midway radius. We can approximate this effect by assuming that the pitch goes to zero over some small distance ε at each end of the coil. Over the remainder of the coil, the pitch increases by an appropriate factor to maintain the azimuthal wrap angle of the coil. This "deflected" configuration is simply a coil with somewhat reduced values of its δ and b/a coil parameters. We then find the difference between the inductance of the coil in its original and deflected states, and divide by the mean deflection of the coil, which we will approximate by $\varepsilon / 2$, to obtain an approximation for dL/ds. If we use ε = 0.5 cm (2.5% of the coil's radial extent), and use Atheta to compute the two inductance values (with the coil parameters of the Z-like system design), we obtain $dL/ds \cong 12$ nH/cm . If we assume that the current in the late phase starts at the peak current observed in the transformer circuit model (5.5 MA) and decays exponentially with a 1 μs e-folding time, we find that $\psi \approx 1.5 \times 10^7$ ampere^2-seconds. Combining these two estimates we find that the impulse is on the order of 18 Newton-seconds, with a corresponding energy deposited in the two primary coils of ~80 Joules.

While the late-time energy deposition appears to an order of magnitude higher than the early-time deposition, it should be noted that our analysis assumed that magnetic flux was trapped in the system because of vacuum insulator flashover. If the insulator does not flash, this will be substantially reduced. Moreover, we believe transformer systems may be favorably predisposed to avoid insulator flashover. In Z experiments, the collapse of the impedance across the convolute traps a large amount of magnetic flux in a rather small inductance. Because of this, the system attempts to make an appreciable voltage reversal on the insulator. In a transformer system, the inductance inside the insulator should go to $L_0 + L_p + L_s + 2M$ (~577 nH for system modeled here), driving a much lower power pulse back into the driver's water section.

3.0 A PROTOTYPE TRANSFORMER EXPERIMENT

In order to validate our modeling of transformer systems, a part of this project was to design and field a prototype transformer. Given the constraints of time, cost, and availability, we chose to perform this work on Sandia's Tesla accelerator. Although not ideal for this application, we can use it to test most of the issues regarding transformer performance. Perhaps the biggest limitation imposed by Tesla is that although it provides two feed lines, they are stacked in parallel rather than in series. To use a symmetric double-sided auto transformer, like the one shown schematically in Fig. 4, the feeds must be in series. In fact, if the feeds are in parallel, the transformer coupling cancels the current in the secondary circuit, resulting in zero output current. However, it turns out that if the symmetry is broken, a transformer that provides current multiplication can be designed. However, in this design only one of the two feeds can be configured as an auto transformer.

3.1 Designing a Transformer for Tesla

Fig. 31 provides a schematic of the circuit for a transformer that could be fielded on Tesla. Note that the two transmission lines on the primary side of the transformer, with currents I_a and I_b, are connected in parallel, with total current $I_p \equiv I_a + I_b$. A detailed analysis of this circuit can be found in Section C.4 of Appendix C. In this section we describe the design of a transformer that effectively adds the currents of the two input transmission lines without a convolute, and then multiplies the sum of the two currents by some factor, which we have chosen to be four in the limit of ideal transformer coupling.

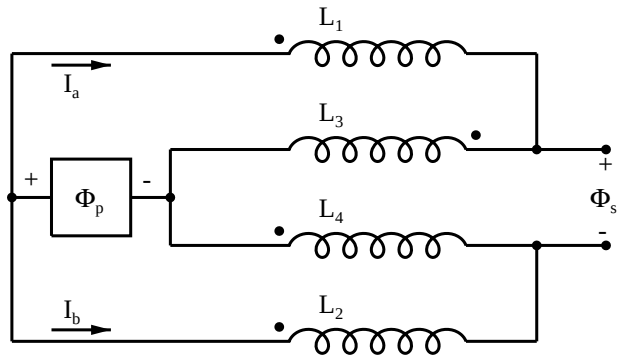

Figure 31. Circuit diagram of parallel-driven transformer system for Tesla.

It is instructive to first consider an ideal 4:1 transformer. Here, by 4:1, we mean that the output current of the device will be four times the *sum* of the two input currents, i.e., $I_s = 4I_p$. Based on the spatial constraints of Tesla's vacuum chamber, reasonable dimensions for the transformer coils, a = 15 cm, b = 30 cm, and S = 5 cm (see Fig. 5), were chosen. At this point, we don't need to specify the axial spacing between the coils (g_p and g_s) since these gaps approach zero in the ideal limit. It can be shown that a 4:1 ideal transformer in this configuration can be achieved by adjusting the wrap angle of the four coils (represented in Fig. 31 by the four inductors) so that the total wrap angle in each of the primary circuits is four times the total wrap angle of the coils in the secondary circuit, i.e., $\Delta\theta_1 + \Delta\theta_3 = \Delta\theta_2 + \Delta\theta_4 = 4\left(\Delta\theta_3 + \Delta\theta_4\right)$. Here we will choose one solution to this relationship: $\Delta\theta_1 = 3\Delta\theta_3$, $\Delta\theta_2 = 4\Delta\theta_3$, and $\Delta\theta_4 = 0$. Using the appropriate value from Table B1, $\Delta\theta_3 = 0.92$ yields $L_1 = 90\,\text{nH}$, $L_2 = 160\,\text{nH}$, $L_3 = 10\,\text{nH}$, and $L_4 = 0$. For an ideal transformer, the mutual inductance between two coils is simply the square root of the product of their self inductances. Consequently, $M_{12} = 120\,\text{nH}$, $M_{13} = 30\,\text{nH}$,

$M_{23} = 40\,\text{nH}$, and $M_{14} = M_{24} = M_{34} = 0$, where M_{ij} is the mutual inductance between coils *i* and *j*.

If these values are applied to (C28), (C30), and (C31) in Section C.4 of Appendix C, one can obtain

$$\Phi_p = 160.0 I_p - 40.0 I_s = 4.0\Phi_s \text{ and } I_s = 4 I_p - 0.1\Phi_s .$$

Thus the output current into a short circuit ($\Phi_s = 0$) would be for times the *sum* of the two input currents, or eight times the average of the two input currents. Note that to the extent there is any flux in the secondary circuit, this value is reduced.

Since the transformer can be ideal only in the limit that the gaps between the coils are zero, in practice transformers will necessarily be non ideal. In addition, the transformer also includes inductance due to azimuthal magnetic fields which further reduce its efficiency from the ideal limit. Using the coil parameters described it the preceding paragraphs, we will now look at the performance of a realizable system. At this point, inter-coil gaps must be specified — we will select g_p = 15 mm and g_s = 7.5 mm (see Fig. 5) for the present. We will use the linear approximation for mutual inductance as a function of spacing described in (B12) of Appendix B, using values of $\mathcal{L}_0$ and κ from Tables B1 and B2. Table 1 shows the values of the non-zero self and mutual inductances obtained using these parameters. It contains three rows; in the first, the self inductance values do not include inductance due to B_θ, the second row does include this inductance, and the third row also includes the inductance of Tesla's power feed structure. There are two things to note regarding the values in the first row. First, the mutual inductances are reduced from their ideal values give above. This effect is most pronounced for M_{12}, since these two coils have the largest separation of any pair of coils in the system. Also, the self inductance values are slightly higher than those used in the ideal case above, due to a slightly higher value of $\Delta\theta_3 = 0.94$, corresponding to the base wrap angle that was used for all the coils fabricated for the actual experiment.

Table 1. Self and Mutual inductances for non-ideal transformer model.

nH	L_1	L_2	L_3	M_{12}	M_{13}	M_{23}
without B_θ	93.3	166.9	10.4	57.8	24.6	28.2
with B_θ	99.0	172.0	12.6	57.8	24.6	28.2
with B_θ & feed	127.5	190.5	12.6	57.8	24.6	28.2

Two "cold" (without electron emission) EM field simulations were performed, using Quicksilver, to test the accuracy of this analytic model. In both, care was taken to accurately model the geometry of the system to match the parameters in the second row (with B_θ) of Table 1. In the first simulation, the load in the secondary circuit was an open circuit, which was accomplished by allowing the two conductors of the secondary circuit to extend all the way to the cylindrical axis without any connection. In the second simulation, the secondary circuit was connected to a shorted coaxial transmission line with a calculated inductance of 7.604 nH from the location in the secondary circuit at which the simulation computed the voltage between the

two secondary electrodes. Using the model described in Section C.4, several parameters for the circuit can be determined, which can be compared to data obtained from the two simulations. In the simulations, currents are measured by integrating the azimuthal magnetic field in θ at appropriate locations, and magnetic flux is obtained by integrating the electric field between electrodes to obtain voltage, and then integrating this over time. Table 2 shows the model predictions and corresponding values measured from the simulation for these two cases. Since this is a linear system, it is convenient to normalize the data to the sum of the two primary currents ($I_p = I_a + I_b$). Since $\Phi_{load} = L_{load} I_s$, the load inductance can be measured from the simulation data by dividing Φ_s/I_p by I_s/I_p, yielding a value of 7.62 nH compared to the calculated value of 7.604 nH.

Table 2. Comparison of Tesla circuit model predictions and Quicksilver simulations for selected circuit parameters.

circuit parameter	Open circuit load		7.604 nH load	
	Model	Simulation	Model	Simulation
Φ_p/I_p (L_{eff})	125.4 nH	123.7 nH	74.3 nH	75.0 nH
Φ_s/I_p (Φ_{load}/I_p)	31.9 nH	30.4 nH	12.2 nH	12.4 nH
I_a/I_p	0.542	0.545	0.610	0.610
I_b/I_p	0.458	0.455	0.390	0.390
I_s/I_p	0.0	0.0	1.600	1.622

Figs. 32, 33, 34, and 35 show the five circuit parameters in Table 2 as a function of the load inductance. The solid curves show the model predictions for the non-ideal transformer. For comparison, the dashed curves show the model predictions for the ideal transformer described earlier. The horizontal lines between 30 and 40 nH indicate the asymptotic value of the parameter for an open-circuit load ($L_{load} \to \infty$). The red circles show the corresponding values obtained from the Quicksilver simulation (see Table 2), where the open-circuit values are plotted at L_{load} = 32 nH. Fig. 32 shows the ratio of secondary current to the total primary current. For this case, the secondary current is zero for the open-circuit load. Fig. 33 shows the fraction of the total primary current that is in each primary input line. Note that these two values are indeterminate for an ideal transformer, since this implies that there is no axial separation between any of the four coils, and consequently there is no way of knowing which coil carries what current. Fig. 34 shows the ratio of total magnetic flux in the primary circuits to total primary current, which is, by definition, the effective inductance L_{eff} seen by the primary circuit's source. Fig. 35 shows the ratio of magnetic flux in the secondary circuit to total primary current.

The reasonable agreement between the model predictions and simulations give us confidence in our predictive ability for the initial design of a transformer. A final design will depend upon holding electron losses to acceptable levels, and for this our quantitative tools are simulations and experiments.

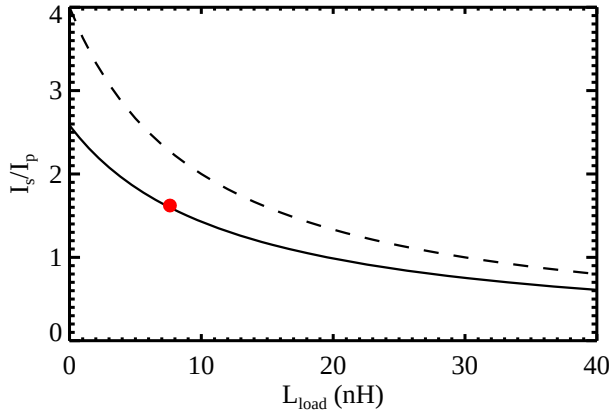

Figure 32. Ratio of secondary current to sum of the primary currents for ideal (solid) and non-ideal (dashed) 4:1 transformer. Red circle indicates value measured from EM simulation.

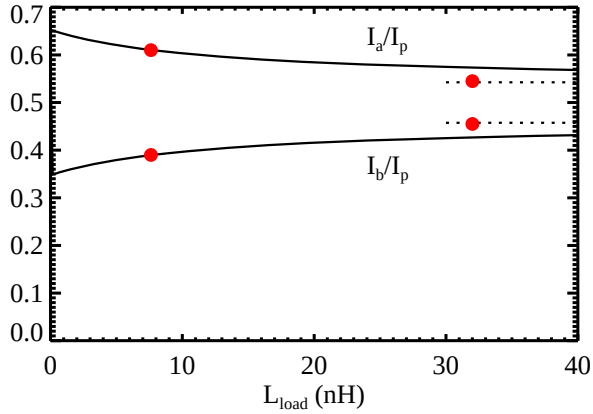

Figure 33. Fraction of primary current in each primary line. Horizontal dotted lines on right indicate asymptotic open-circuit values. Red circles indicate values measured from EM simulation (open-circuit values at L_{load} = 32 nH).

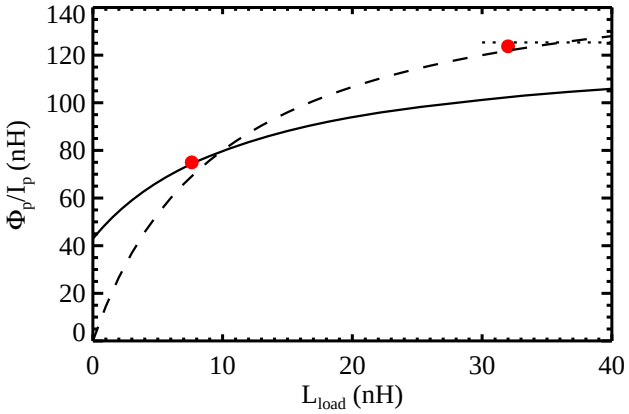

Figure 34. Ratio of primary flux to total primary current (L_{eff}) for ideal (solid) and non-ideal (dashed) 4:1 transformer. Horizontal dotted lines on right indicate asymptotic open-circuit values. Red circles indicate values measured from EM simulation (open-circuit values at L_{load} = 32 nH).

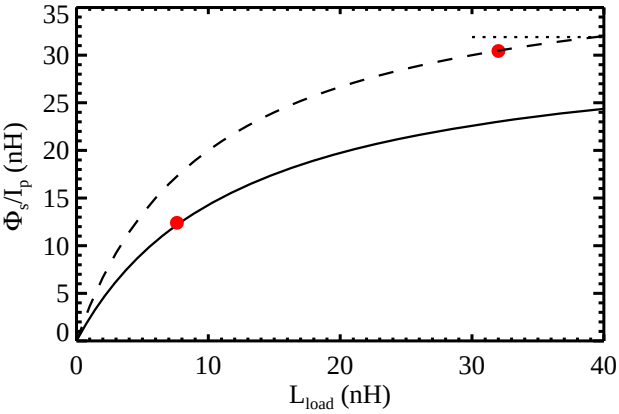

Figure 35. Ratio of secondary flux to total primary current for ideal (solid) and non-ideal (dashed) 4:1 transformer. Horizontal dotted lines on right indicate asymptotic open-circuit values. Red circles indicate values measured from EM simulation (open-circuit values at L_{load} = 32 nH).

3.2 Fabrication of Hardware and Execution of Tesla Experiment

Tesla, a small pulsed power driver, provided the energy for the transformer excitation. The system consisted of a 24-stage Marx generator charged to ±60 kilovolts, an intermediate store capacitor switched by an electrically-triggered gas switch, and four pulse-forming water-insulated transmission lines. Each of the four pulse-forming lines was independently switched by self-closing water switches. Fig. 36 shows a sectional view of the system.

The typical driver output was a ~800 kV peak amplitude forward wave in the four 7.8Ω lines, for a net impedance of 1.95Ω. The full-width at half-maximum of the forward going wave was 53 ns. Into the ~90 nH of the feed and one configuration of the coil system, the system delivered ~680 kA with 31 ns 10-90 rise time. Fig. 37 shows the installation of a transformer coil into the driver system.

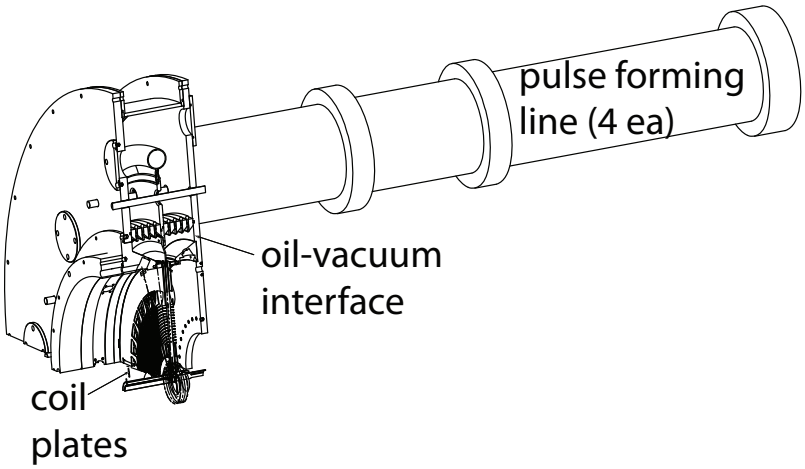

Figure 36. Sectional view of the transformer system and the pulsed power driver.

The driver system had its oil-plastic-vacuum interface at 61 cm radius. The axial height of the insulator had 10 cm of active insulator and 1.2 cm of metal grading rings. This insulator did not flash during any of the transformer tests. The insulator system was in a balanced feed geometry, with the high voltage electrode surrounded by equal height insulator assemblies. The power feed was thus two sided. The transformer hardware was designed to use both sides of the feed, because that effectively lowers the source inductance and improves the driver system efficiency.

Figure 37. Installation of a primary coil into the pulsed power driver system.

The inductance reflected on the primary feed was of the order 100 to 200 nH. The time constant L_{load}/Z_{driver} (where L_{load} is the total inductance seen by the driver, and Z_{driver} is the driver source impedance) was therefore 50-100 ns. The coil inductance (rather than the driver impedance) predominately determined the current over the duration of the 50 ns drive pulse. At the voltages used in the system, the cathode surfaces could freely emit electrons. In that case, there is another significant time constant. At the outer diameter of the coil feed, the feed gap can act as a shunt electron beam load. The time over which that shunt load dictates current is given by L_{load}/Z_{shunt} (where Z_{shunt} is the impedance of the electron beam current shunt). The electron beam shunt impedance can be approximated by $Z_{shunt} \cong 60(g/r)$, where g is the gap and r is the radius. For a 10 mm axial gap at 400 mm radius, the shunt impedance is ~1.5 Ω, and the system has two such gaps in parallel. The time constant is therefore 130 ns for 100 nH load inductance reflected to the primary. The shunt

electron beam load can be significant, especially for the relatively fast 50 ns pulse used to drive the experiment.

3.2.1 Coil Fabrication

The coils were fabricated from 14 gauge (1.9 mm) thick 304L stainless steel. The coil design was transferred to the Solidworks mechanical design program in radius and angle points for one cut, and duplicated and rotated to create the desired multiple vane coil geometry. The coils were cut from flat sheet steel. The parts were fabricated from design files.

The coil fabrication options considered were conventional machining, electric discharge machining, and laser cutting. Conventional machining would induce considerable stress into the finished coils. Because of the high voltages, the coils could not be supported with insulators, and must maintain the required flatness (~10% of the gap width, or less than one millimeter) restrained only at the center and outer periphery.

The stresses imparted to the material with conventional machining would likely render the coils unable to maintain flatness in the unrestrained state. Electric discharge machining (EDM) would not induce significant mechanical or thermal stress, but no EDM machines were available large enough to produce the parts considered here. Laser cutting imparts no mechanical stress and little thermal stress. Laser cutting was the method chosen to produce the parts. It is likely that water jet cutting would also be able to produce the parts with tolerable induced mechanical stress, and may be a less expensive way to build such coils. The cost of the laser cut coils was about $4k apiece, which is cheaper than conventional machining and much less expensive than EDM.

Laser cutting may not scale effectively to the thicker plates likely needed for a transformer on a multi-megampere driver. For thicker plates, water jet cutting would be cost effective and can be done with quarter millimeter accuracy. No capability (apart from conventional machining) has been identified for conical shaped coils. Conical coils might have some topological benefit, and would certainly have strength advantages over flat plates.

3.2.2 Benchtop Results

The intent of the benchtop testing was to test the transformer concept with gaps smaller than could have been done reliably in the machine, and with varied inductances and power flow configurations. The relative ease with which the bench top testing could be done was an advantage. Fig. 38 shows the two views of the hardware set up for benchtop testing.

To use and calibrate the current measuring diagnostics required reasonable signal levels (greater than 20 mV) that could be recorded on digitizers. The diagnostic signal level is proportional to the time derivative of current. This is helped with both high voltage and low impedance. Minimization of shield-current-induced cable noise also makes a relatively fast pulse desirable. For these reasons, the bench top excitation was done using an available 2Ω, 40 ns, 10 kV pulse generator often used for calibrations on similar systems. The pulse is transported on

sixteen cables. Each of the cables is 30Ω. The cable two-way transit times are longer than the pulse duration, so the source is modeled well as a simple resistively-limited source.

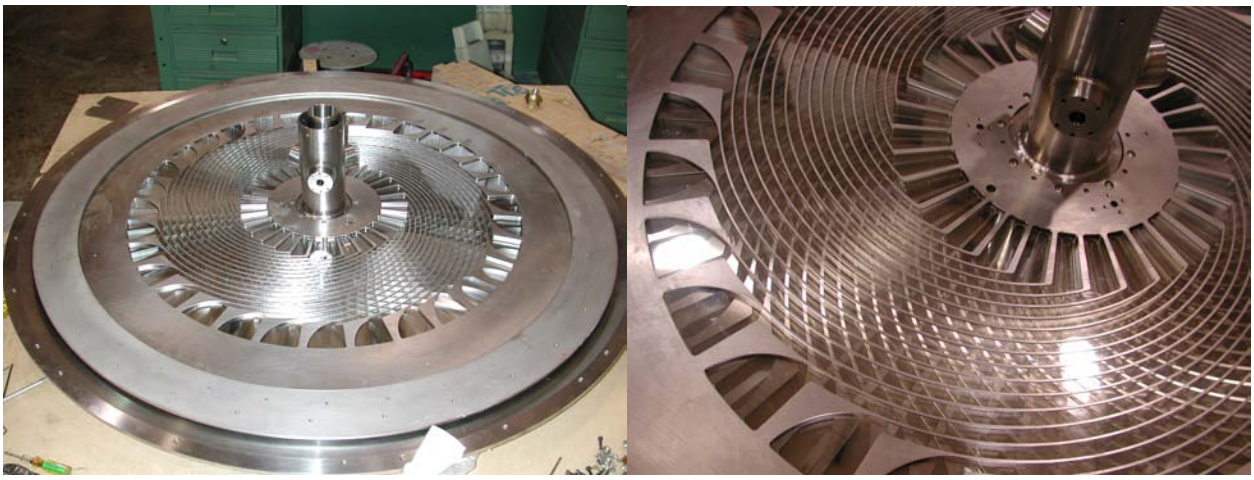

Figure 38. Views of the transformer system assembled on a workbench.

3.2.3 Diagnostics

The primary diagnostics were current measurements in vacuum. The driver current was measured upstream of both primary coils in a high impedance region of the vacuum feed. The primary coils had current monitors installed downstream of the azimuthally pitched regions on their anode sides. The load inductor had three current monitors on the anode side. The signals propagated along 5.8 meter long RG223 jumpers to the air-vacuum feed-through plate, through an inductive isolator. The isolator inductance was about 1μH total and 16 ns in length. In air, the signals traveled on half-inch Foamflex of 7.6 meter length. Fig. 39 shows the location of the monitors in the experiment.

The signal monitors were all derivative responding. The primary current monitors consisted of single turn flux loops recessed into the coil plates. The secondary current monitors were larger area single turn loops deeply recessed into the anode coaxial region. The signals were integrated with high quality passive integrators. The passive integrators were calibrated to determine the integrating time constant. Using resistors rated for 7 kV in the integrators made the integrators robust against applied high voltages. The integrators had a nominal 2.2 μs time constant,

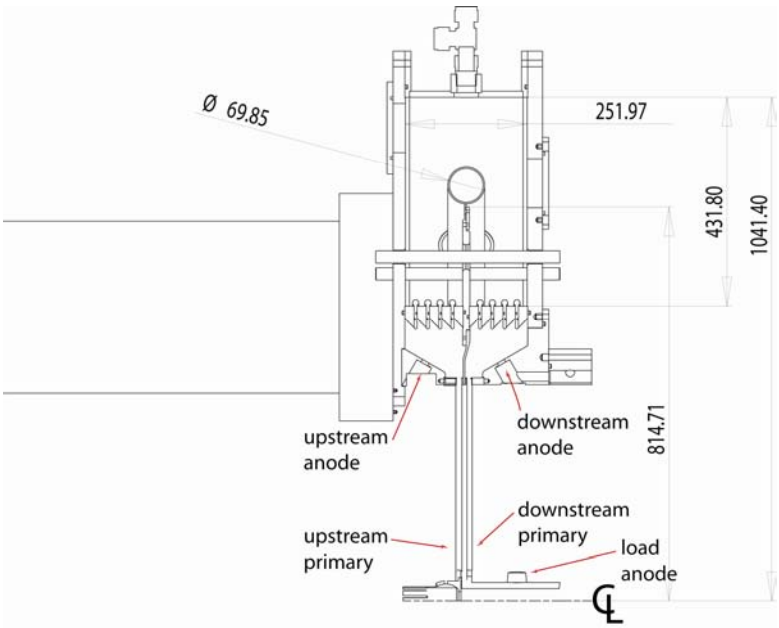

Figure 39. Location of diagnostic monitors. Dimensions in mm.

so attenuators were not necessary.

The transformer signal monitors were at elevated potential from ground. The signals cables were routed through an inductive isolator system. The isolator had 1 μH inductance (8 ns at 115Ω and 8 ns at 17Ω) and so carried of order 20 kA peak during the first voltage pulse on high voltage experiments. Some of the signals were exposed to considerable magnetic flux, and so had issues with shield-current-driven voltages. This was minimized with copper braid, but some signals were driven spuriously later in time. This is due to a signal proportional to current penetrating the signal cables with a few hundred nanosecond time constant. The integration of this along with the desired signal results in signals being unreasonable after two hundred nanoseconds or so. This process is generally unstoppable in low impedance large systems, but the time constant for flux penetration can be maximized with large ground conductors and high quality connectors.

3.2.4 Calibrations

The calibrations were done two ways. First, the coils and load inductor were assembled on a table. The coils as machined were not perfectly flat in the unrestrained condition. With the coil axes vertical, plastic sheets were placed between the plates to maintain separation. With the separation maintained by spacers, the smallest gaps could be tested more easily than in the driver setup with only vacuum insulation. Second, the monitors were calibrated after installation into the driver setup. The technique was the same — flow a known current past the monitors to be calibrated. In some cases this was easily accomplished. In other cases, displacement current due to inter-coil capacitance made the calibrations more difficult.

The coils have substantial capacitance because of the relatively large, closely spaced plates. Disks of 400 mm radius and 7 mm gap spacing would have 636 pF in vacuum. With plastic between the plates, the capacitance would rise to 1.6 nF. The impedance, $Z = (L/C)^{1/2}$, is about 5.5Ω. Since this is comparable to the calibration pulser source impedance of 2Ω, and the $(LC)^{1/2}$ time of 5.5 ns is comparable to the 15 ns rise time of the calibration pulser, the calibration data were substantially affected by this capacitance. The monitors downstream of the coil plates measured current flowing in the output end of the coil, but the reference monitor upstream of the coil recorded displacement current in addition to direct current flow.

Fig. 40 shows a typical calibration result for a load anode current monitor. The reference was a 0.01Ω current-viewing resistor on one of the pulser output cables. The capacitance between the reference monitor and the monitor being calibrated was small in this case. The relatively small current-viewing resistor (0.01Ω) compared

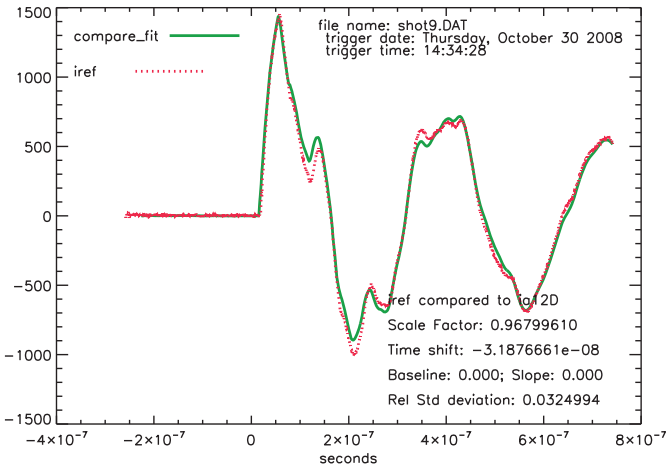

Figure 40. Typical calibration of load anode monitors. the reference is a 0.01Ω current-viewing resistor on one of the sixteen drive cables.

to the 30Ω cable means the current viewing resistor does not affect the current distribution. The total current is calculated by multiplying the current measured on the one cable by the number of cables.

3.2.5 High voltage experiments

As stated previously, each of Tesla's four pulse forming lines can be independently switched by self-closing water switches. The gap of the water switches could be varied. For this experiment, the Marx charge was not varied to avoid changing the operating points of the Marx generator and the gas switch. At the largest water switch gaps, the upstream line reached its highest voltage before the water switch closes. This gives the highest amplitude, shortest forward-going pulse. With the water switch gaps set smaller, the upstream line voltage does not reach as high a voltage, and energy continues to flow from the upstream system for longer times. Thus, the smaller gaps resulted in a lower amplitude, but longer duration pulse.

The driver output was a ~800 kV peak amplitude forward wave in the four 7.8Ω lines, for a net impedance of 1.95Ω. The full-width at half-maximum of the forward going wave was 53 ns. Into the ~90 nH of the feed and coil system, the system delivers ~680 kA with 31 ns 10-90 rise time.

Fig. 41 shows a picture of a long azimuthal wrap coil installed in the driver. The coil strength decreases with wrap; this coil required support at all times. The coil system as a unit was self-supporting, but additional support pieces were needed during the assembly process.

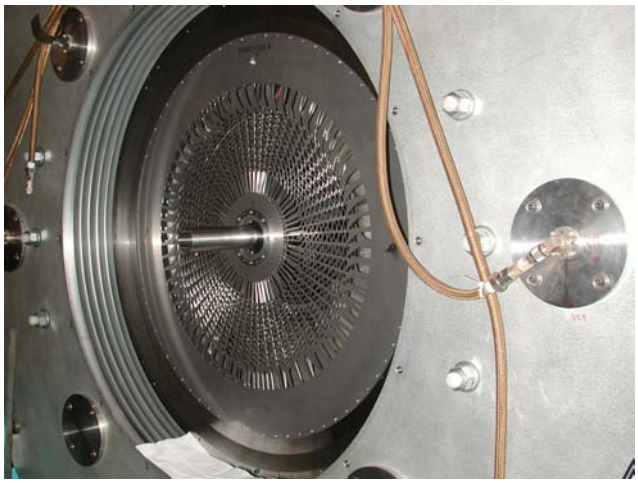

Figure 41. The two upstream coils installed in the machine.

Table 3 lists the configuration for the tests. The coils themselves were not changed; only the inter-coil gap spacing was varied. The water switch gap controls the amplitude of the forward going voltage pulse. The smaller water switch gap results in a lower amplitude output pulse.

Current was measured in vacuum, on the anode side, with eight flux loops recessed into the anode conductor. The gap in the region in which the monitors was located was substantially larger than the smallest vacuum gaps, and the electron flow in the monitor region was small. Voltage was measured on the oil side of the vacuum insulator with D-dot sensors.

Table 3. Configuration of Experiments.

Shot numbers	primary gap (center to center)	secondary gaps	Water switch gaps	geometric shunt loss (Ω)	Empirical loss (Ω)
568-570	10	10	40	0.61	0.6
571-574	10	10	19	0.61	
575-576	12.5	5	19	0.80	
577-578	12.5	5	40	0.80	0.9
579-580	17.5	5	40	1.17	2.7
581-582	17.5	5	19	1.17	
584-586	15	7.5	19	0.98	
587-589	15	7.5	40	0.98	1.1

3.3 Data Analysis and Comparison to EM PIC Simulation

3.3.1 Initial Observations of Tesla Data

Fig 42 shows currents measured on a test with 10 mm primary and secondary gaps. The losses (primary currents compared to total drive current) are relatively large. Fig. 43 shows current with 15 mm primary gaps and 7.5 mm secondary gap. Note that the secondary impedance is much lower and so electron flow and losses can be tolerable in the secondary with much smaller gaps than in the primary. Fig. 44 shows current measured with 17.5 mm primary gaps and 5 mm secondary gaps. The secondary current is a higher fraction of the machine drive current.

The system has a time constant determined by the reflected inductance and the shunt e-beam impedance at the transformer input. This time compared to the pulse duration to some extent determines the losses.

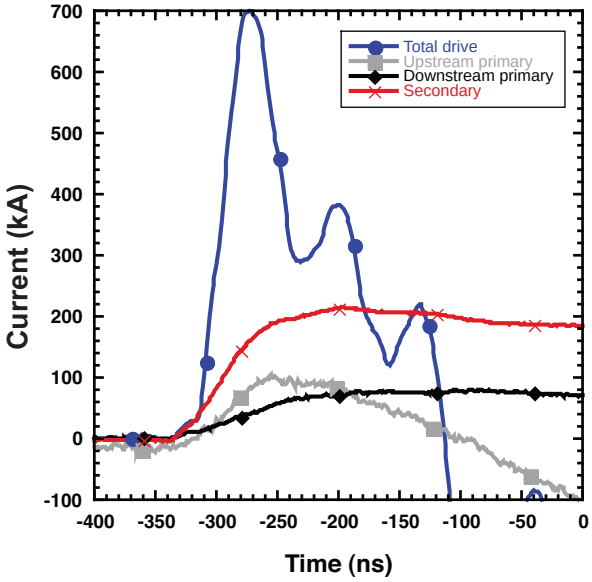

Figure 42. Current on high voltage experiment with 10 mm (center-to-center) primary and 10 mm secondary gaps (shot 570).

With the measured forward wave in the water pulse forming lines, we can calculate analytically the current in a fixed inductor. We can add a shunt resistor to the model to account for the electron beam load. While the electron beam load does not behave exactly as a fixed resistor, it is possible to fit the data reasonably well with static components. Fig. 45 shows total drive current, measured primary current, and results from an analytic calculation based on the forward going wave and static inductance and resistance. The resistance value was adjusted to fit

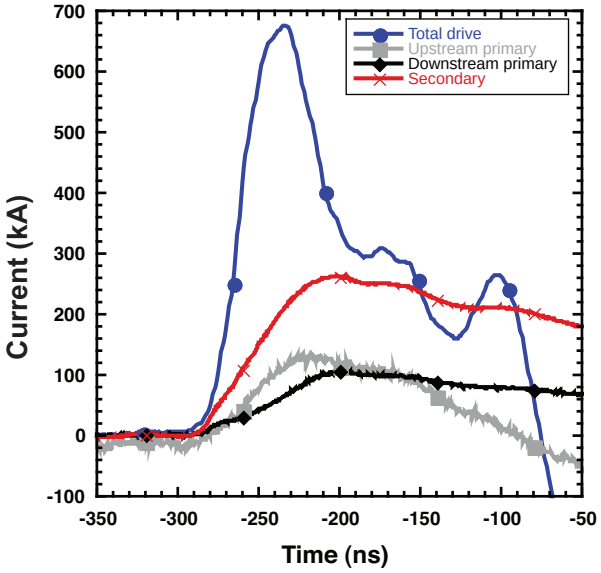

Figure 43. Currents measured with 15 mm center to center primary and 7.5 mm secondary gaps (shot 587).

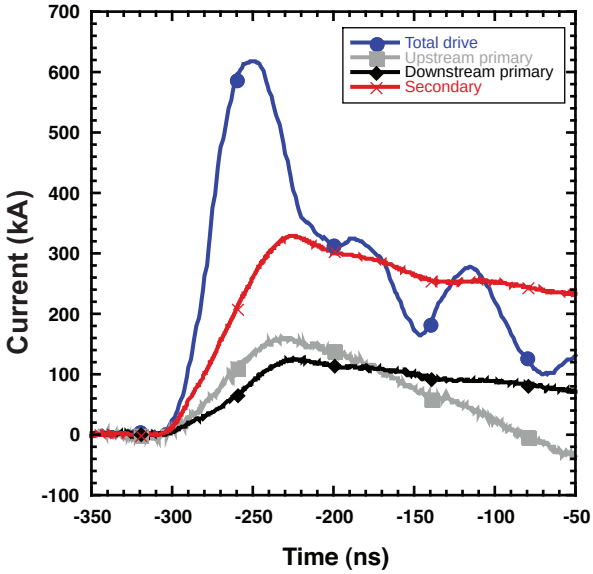

Figure 44. Currents measured with 17.5 mm center to center primary and 5 mm secondary gaps (shot 579).

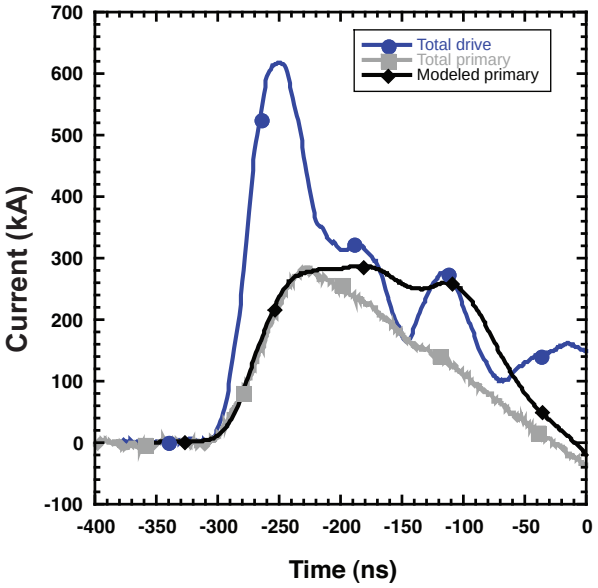

Figure 45. Measured total drive current and primary current. Also shown is a calculation with static component values showing a reasonable fit with 2.7Ω shunt impedance (shot 579).

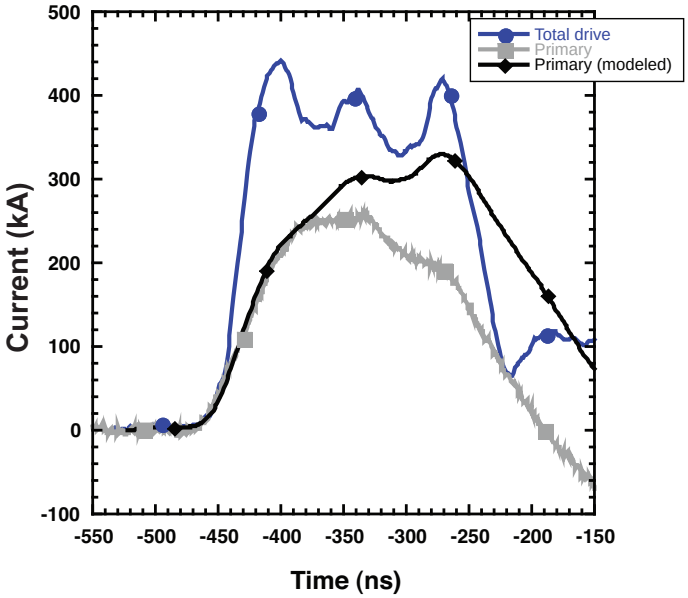

Figure 46. The driver and primary currents for the largest primary gap at the lower machine drive level. Also shown is a static component calculation with 2.7Ω shunt impedance. With the larger gaps and the longer pulse, the secondary current reaches the highest fraction of total machine current.

the rise of the primary current. For this test, a value of 2.7Ω provided a reasonable fit during the rise. The data are affected late in time by shield current and falling impedance of the electron beam shunt. Fig. 46 shows results for the same gap configuration, but with a lower drive longer pulse, and so losses are even less important.

Fig. 47 shows the geometric impedance, $Z = 60(g/r)$, (two in parallel) and the empirically-fit shunt impedance versus primary center-to-center gap spacing. At small gaps, the shunt impedance dominates current flow and the fit value agrees closely with the geometric value. At larger gaps, the loss is less important and more current flows past the shunt. Because of magnetic insulation, the shunt value can be higher than the geometric impedance.

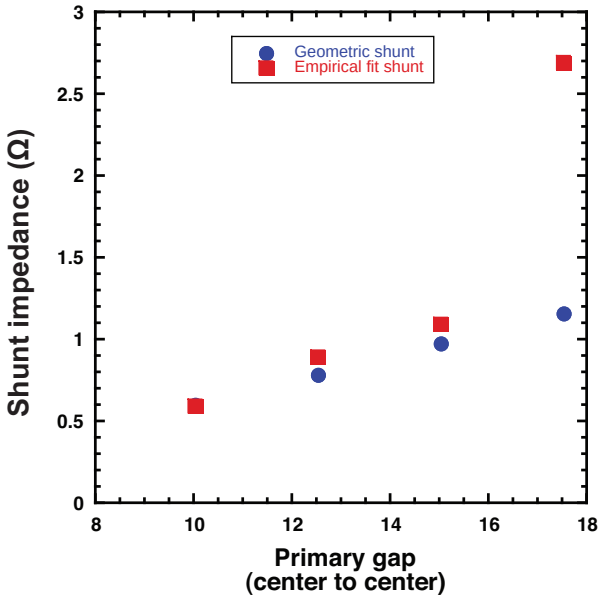

Figure 47. Geometric impedance and empirically fit shunt resistance versus primary gap. Because of magnetic insulation, the shunt resistance exceeds the geometric impedance when substantial current flows past the shunt location.

3.3.2 Comparison of 2D PIC Simulation to Tesla Experiment Data

Two of the Tesla experimental configurations were simulated. These groups were shots 579 through 582, with 17.5 mm primary gaps and a 5.0 mm secondary gap, and shots 587 through 589, with 15.0 mm primary gaps and 7.5 mm secondary gap (see Table 3). We will compare the experimental currents to shots 579 and 587. In these experiments the current measurements in the transformer were located in a region that went to full machine voltage during the shot. As a result the cabling was carried to the data recording enclosure via an inductive isolator. The inductance amounted to a shunt inductor across the high pitch primary coil. Such an inductor was added to the simulation with a value of 1.3 μH. The actual value of this inductor was not more than that value, and might possibly have been half that value, but not less.

Figure 48 shows an overlay of the measured and the simulated currents for shot 579. Currents measured at five locations (see Fig. 39) are compared. We will use the notation from the Tesla design section of this report (Section 3.1), in which the two primary lines are denoted by *A* and *B*. In the

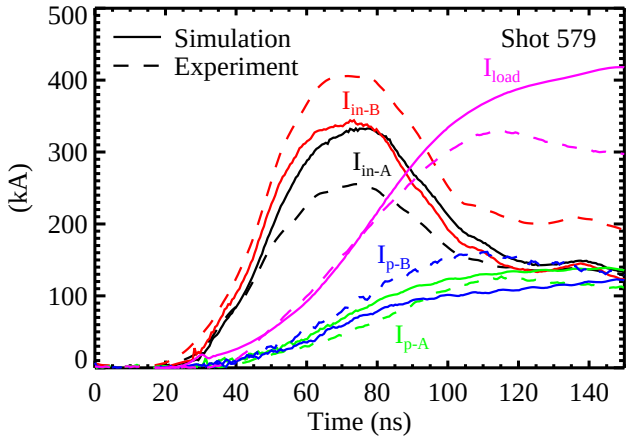

Figure 48. Comparison between simulation and experimental measurements of currents at five locations for shot 579.

nomenclature of the experiment, these are *downstream* and *upstream*, respectively. For example, the input currents $I_{in\text{-}A}$ and $I_{in\text{-}B}$ correspond the measurement locations (on Fig. 39) *downstream anode* and *upstream anode*, respectively. Similarly, $I_{p\text{-}A}$, $I_{p\text{-}B}$, and I_{load} correspond to experimental measurement denoted *downstream primary*, *upstream primary*, and *load anode*, respectively. The input currents in the simulation are measured at the outer radius of the modeled region at 45 cm. The other three simulation currents are measured at the exact location of the experimental measurement. In the figure, each of the five currents is color-coded, and the line type is used to indicate whether the current is from the simulation or the experiment.

The simulated *A* and *B* input currents are nearly equal in the simulation, whereas the *B* (upstream) currents are appreciably higher in the experiment. The averages of the two are in excellent agreement (see Fig. 49), so the driver model, and the circuit model exterior to the transformer do not cause the discrepancy. From the difference between the input currents and the currents measured in the primary coils, the loss at the *B* input is much larger than at the *A* input.

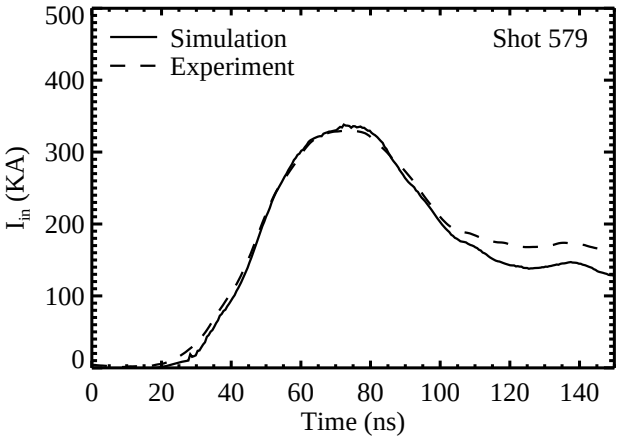

Figure 49. Comparison of averages of *A* and *B* input currents for simulation and experiment for shot 579.

The four primary currents are in substantial agreement, but a careful look tells us that the balance between *A* and *B* is wrong. In the simulation, the *A* current is higher than the *B* current, as was expected from the circuit model calculations described in Appendix C.4. Shunting of the *B* coil by the inductive isolator brings the *B* closer to the *A* current. If the inductance of the isolator were half the value used in the simulation, these two currents would be closer together, but still would not agree with the measurements.

This disagreement probably is not due to just one problem. It may be that the excessive electron loss current in *B* is caused by some difference in the gaps at the transformer inputs. The gaps are small, and a small change in the gaps due to vacuum pump-down or some other similar effect might explain this.

Because of its location, cabling for signal $I_{p\text{-}B}$ follows a different route than others. There are clear errors in the late time $I_{p\text{-}B}$ signal, and the problems causing these errors may occur earlier than is apparent. Certainly that signal is well above the other primary signals from early in the pulse. An error even early in time might explain that discrepancy.

The load currents are in reasonable agreement. Because their shapes are similar until late in time, they were used to align the two sets of data, so the timing agreement was bound to occur.

Figures 50 and 51 show the same data recordings for the experiment with 15.0 mm primary gaps and 7.5 mm secondary gap. The data looks much the same as the previous case, except that $I_{p\text{-}B}$ is in even greater disagreement with the other primary currents. Figure 52a shows the

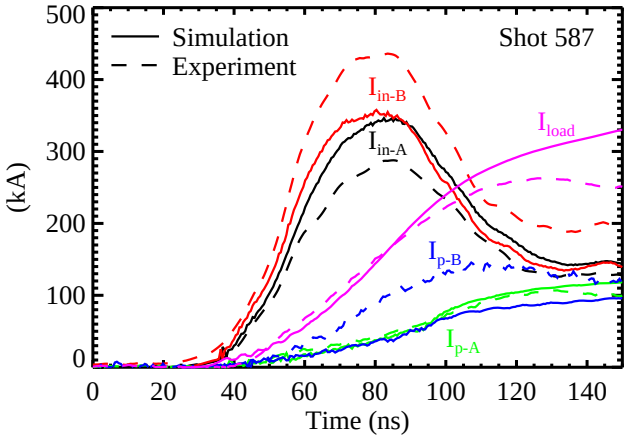

Figure 50. Comparison between simulation and experimental measurements of currents at five locations for shot 587.

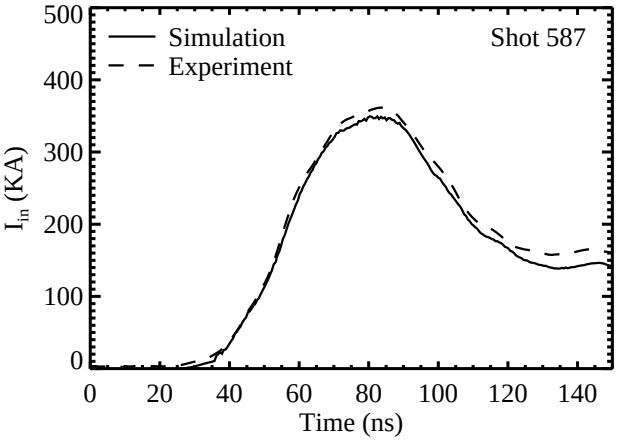

Figure 51. Comparison of averages of *A* and *B* input currents for simulation and experiment for shot 587.

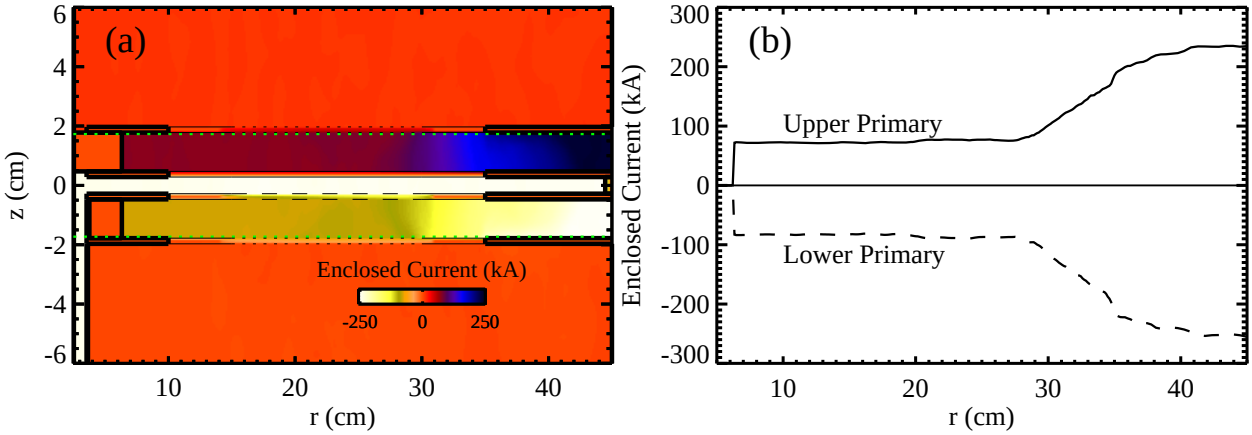

Figure 52. Simulation enclosed current for Tesla shot 587. (b) shows radial variation of the enclosed at two axial locations, indicated by the green horizontal dotted lines in (a).

enclosed currents in the transformer region. Fig. 52b shows the enclosed current at two axial locations (indicated by the two dotted green lines in 52a) near the anode surfaces of the two primary lines. Notice that the currents flow the opposite way in *z* because of this transformer's parallel configuration. The currents are lost in much the same way on the two sides, with no sign of electron recapture on either primary coil as occurred on the bottom coil in the Z simulations (see Section 2.3.1).

Because of the limited resources available for this experiment, there was only a single run of 22 shots, and no time for modifications followed by further experiments. Little could be done to reduce the outer electron loss current because the Tesla machine has a small gap at the outer radius of the transformer.

There are a few clear conclusions that can be reached when considering this experiment. With regard to total electron loss, simulation and experiment are in complete agreement. If the problem is that the gap was too small on one side, and too large by the same amount on the other side, this would explain those data.

The coils did survive with no visible distortion due to the large currents they carried. Moreover, in spite of the large amount of electron loss, there was no damage from arcs. Since a gas breakdown of desorbed gas would concentrate current into arcs, such a breakdown does not appear to have happened. Observed uniform discoloration on anode surfaces appeared to be due to electron loss or very low pressure gas.

The imbalance in primary currents cannot be explained from the data. As mentioned earlier, the signal $I_{p\text{-}B}$ had a very large negative excursion, indicating -1.2 MA late in time. If it were assumed that this signal is faulty from the beginning and consequently ignored, and if the disparity in electron loss between the two sides were attributed to a difference in the *A* and *B* feed gaps, the simulation and the experiment are in agreement. Unfortunately, there is no way for us to resolve this question without further experiments.

4.0 CONCLUSIONS

This project evaluated the merits of transformer technology to replace existing convolute current adder technology. A staged approach using analysis, computation, and experiment was used to address issues step-by-step, allowing incremental evaluation of the concept's viability. The projects ultimate goal was to field an experiment showing the benefits of this concept for next-generation pulsed-power drivers.

4.1 Summary of Accomplishments

We have made a study of transformer inductance and efficiency in order to understand the important parameters to be considered when designing coils and how they affect the performance of an overall transformer system. Building upon this work, we have developed accurate circuit models for transformer-based systems, allowing the comparison such a system with Z-like currents and power to the existing convolute system currently fielded on Z. In addition, these tools have provided a basis for the design of a prototype experiment performed on the Tesla accelerator. This also allowed us to quickly evaluate several potential transformer configurations, including auto-transformers, symmetric double auto-transformers, and parallel-fed transformers.

We have developed a two-dimensional coil model and implemented it in the Quicksilver electromagnetic PIC simulation code. This model provides a 2D approximation for this inherently 3D device which has proven to be extremely accurate. This model includes extensive capability to treat the interaction of the coils with charged particles (typically electrons). This model has been applied to the analysis of Z-like transformer-based systems, as well as the prototype transformer experiments performed on Tesla.

Hardware for the Tesla prototype experiment was designed, engineered, fabricated, and then successfully fielded. In addition to the transformer itself, this included components needed to adapt to the Tesla driver, diagnostics, and other miscellaneous items. The coils for the Tesla experiment were intentionally designed to push the mechanical limit, and ultimately proved to perform acceptably. The hardware was designed to allow the independent adjustment of the inter-coil separations in the transformer from 5 to 17.5 mm. Twenty-two high-voltage shots were taken in ten different configurations.

4.2 Significant Results

The project has demonstrated that transformers can provide effective current multiplication for pulsed-power drivers. Acceptable coupling efficiency can be obtained with reasonable inter-coil spacing. We have designed and simulated transformers for both series- and parallel-stacked multi-module drivers, and demonstrated operation on the parallel driver Tesla.

We have also shown that electron losses can be significant and attention must be devoted to the mitigation of this loss. Although we have explored techniques to provide this mitigation, which have resulted in significant reductions to it, we believe that they are still unacceptably

high, and that successful transformer implementations will require further improvement. Having said that, we also believe that such improvement is very likely achievable, and further simulation will help lead us there. Of course, assuming the success in demonstrating sufficient improvement via simulation, eventually well-designed, production-level experiments would be needed to validate these results.

Analysis has shown that the mechanical stress during the time of the experiment is not particularly large, and it should be easy to design coils that can handle this stress. It is likely that late-time stress will be larger, particularly if the vacuum insulator flashes and traps magnetic flux the transformer. However, even in the worst case, the hardware should be affordable enough to be considered "single-shot" or "throwaway."

It should be noted that our analytic models and computational tools have been demonstrated to provide good predictive capability. We believe this to be of critical importance in the design of transformer systems.

4.3 The Future

We believe that it will soon be, if it is not already, important that an alternative for existing post-hole convolute systems be developed. This component is clearly the weak link in efficient power transport from driver to load in present-day systems, and it appears that its problems have only become worse as driver current has increased and load requirement have become more demanding. The root cause of the problem is that the electron loss in convolutes occurs over very small areas corresponding to its magnetic nulls, resulting in ultra-high current densities, and the corresponding electrode heating. They are clearly approaching a performance cliff as current increases, and an alternative will be needed in the future, even possibly for a next-generation driver.

We believe that this project has demonstrated that transformer systems *might* be the answer. Although loss current densities in a transformer system are much lower that those for comparable convolute systems, they are still an issue. However, they could be enough lower to get us to the next-generation machine. The following steps will probably be needed to determine if transformer can live up to this potential:

- Modeling and simulation needed to continue to explore methods to reduce electron losses.
- Use of a transformer rather than a convolute puts different demands on the driver. How to optimize the design of the driver to take advantage to the transformer needs to be considered in an integrated design.
- Modeling and simulation can only take us so far — a larger-scale experiments will eventually be needed.

5.0 REFERENCES

1. C. W. Mendel, Jr., T. D. Pointon, M. E. Savage, D. B. Seidel, I. Magne, and R. Vézinet, "Losses at magnetic nulls in pulsed-power transmission line systems," Physics of Plasmas **13**, 043105, 2006.
2. C. W. Mendel, Jr., J. P. Quintenz, L. P. Mix, D. M. Zagar, R. L. Noack, T. Grasser, and J. A. Webb, "15-cm Hybrid Diode on PBFA-I", Appl. Phys. **62**, 1987.
3. M. E. Savage, D. B. Seidel, C. W. Mendel, Jr., "Design of a Command-Triggered Plasma Opening Switch for Terawatt Applications," IEEE Trans. Plasma Science **28**, 1533-1539, 2000.
4. J. P. Quintenz, D. B. Seidel, M. L. Kiefer, T. D. Pointon, R. S. Coats, S. E. Rosenthal, T. A. Mehlhorn, M. P. Desjarlais, and N. A. Krall, "Simulation Codes for Light-Ion Diode Modeling," Laser Part. Beams **12**, 283-324, 1994.
5. K. Struve, private communication.
6. T. Pointon, W. L. Langston, and M. E. Savage, "Computer Simulations of the Magnetically Insulated Transmission Lines and Post-Hole Convolute of ZR", Proc. 16th IEE Pulsed Power Conf., Albuquerque, NM, p. 165, June 2007.
7. R. W. Lemke, M. D. Knudson, J-P. Davis, D. E. Bliss, and H. C. Harjes, "Self Consistent, 2D Magneto-Hydrodynamic Simulations of Magnetically Driven Flyer Plate Experiments on the Z-Machine," in Shock Compression of Condensed Matter – 2003, M. D. Furnish, Y. M. Gupta, and J. W. Forbes, Ed., American Inst. Phys. 0-7354-0180-0/04, Melville, NY, pp. 1175-1180.
8. L. P. Mix, R. S. Coats, and D. B. Seidel, "PFIDL: Procedures for the Analysis and Visualization of Data Arrays," Tri-Laboratory Engineering Conference on Computational Modeling, Pleasanton, CA, Oct. 31-Nov. 2, 1995.
9. M. E. Cuneo, IEEE Trans. Dielectr. Insul. **6**, 469, 1999.
10. T. W. Sanford, J. A. Halbleib, J. W. Poukey, *et al*., J. Appl. Phys. **66**, 10, 1989.
11. R. A. Vesey, T. D. Pointon, M. E. Cuneo, *et al.*, Phys. Plasmas **8**, 289, 2001.

Appendix A: DISCRETE VANE EFFECTS ON COIL INDUCTANCE

Although the coil wires in general will have some curvature as they wind over the coil's radial extent, their radii of curvature will be large in comparison to the spacing between coil wires. Consequently, we can neglect their curvature for this analysis, and adopt a local 2-D approximation in a plane perpendicular to the wires. To get the inductance per unit length of a wire, we will thus compare a plane of straight wires of radius *a* with center-to-center spacing *b* and each carrying current *I* in the -*z* direction, to a uniform current sheet lying in the same plane and carrying current *I*/*b* per unit width in the same direction.

The line of wires can be described as the sum of the sheet of current plus an array of quadrupole elements. Each element consists of a wire carrying current I in the -*z* direction and a bar of current of width *b* and zero thickness centered on the wire and also lying in the plane *y* = 0. Each slab carries current *I* in the *z* direction, so each quadrupole element carries no net current. Quadrupole element are centered at the locations *x* = *nb* for all integers, *n*. The slabs exactly cancel the layer of current, thus leaving only the current in the wires.

The magnetic field due to the quadrupole element centered at (0,0) generates magnetic field

$$\mathbf{B}_q(x,y) = \frac{\mu_o I}{2\pi}\left[\frac{y\hat{\mathbf{x}} - x\hat{\mathbf{y}}}{x^2+y^2} - \frac{1}{b}\int_{-b/2}^{b/2} \frac{y\hat{\mathbf{x}} - (x-x')\hat{\mathbf{y}}}{(x-x')^2+y^2}\,dx'\right] \tag{A1}$$

The current in the wire has been approximated by a line of current at (0,0). Actually the currents of all the neighboring locations cause the wire to have an additional quadrupole distribution of current with higher current per unit circumference at $(0,\pm a)$ and lower current per unit circumference at $(\pm a,0)$. This can be seen by considering the separatrix for a line of currents *I*. The flux between the separatrix and the wire is the same by any path, but the spacing is much larger in the *x* direction. The effect of this on the distributed inductance is of order $(a/b)^2$, and will be neglected.

We can get all the information we need from B_x, so we won't calculate B_y. Integrating the x component of (A1),

$$B_{q_x} = \frac{\mu_o I}{2\pi}\left[\frac{y}{x^2+y^2} - \frac{1}{b}\left(ctn^{-1}\left(\frac{2y}{b+2x}\right) + ctn^{-1}\left(\frac{2y}{b-2x}\right)\right)\right]. \tag{A2}$$

The integral of (A2) over $x = \pm\infty$ is zero for all *y*, so the net current is zero, as expected.

We need to calculate the flux ϕ_0 due to the quadrupole element at (0,0). There is no flux inside $x^2 + y^2 = a^2$ due to the wire, therefore ϕ_0 is given by

$$\phi_0 = \int_0^{\Lambda b} B_{q_x}(0,y)dy = \frac{\mu_0 I}{2\pi}\left[\ln\left(\frac{\Lambda b}{a}\right) - \int_0^{2\Lambda} ctn^{-1}\eta\, d\eta\right], \tag{A3}$$

where Λ is a large number that will eventually go to infinity. The integral is available in most tables (e.g., Dwight, [1] 528.), and yields

$$\frac{2\pi\phi_0}{\mu_o I} = \ln\left(\frac{b}{2a}\right) - \frac{1}{2}\ln\left(\frac{1+(2\Lambda)^2}{(2\Lambda)^2}\right) - 2\Lambda\, ctn^{-1}(2\Lambda). \tag{A4}$$

Taking the limit as Λ goes to infinity

$$\frac{2\pi\phi_0}{\mu_o I} = \ln\left(\frac{b}{2a}\right) - 1. \tag{A5}$$

We have neglected the quadrupole current distribution on the surface of the wire centered at (0,0).

Defining the field due to the two quadrupole elements at $x = \pm nb$ by $B_{xq_n}(x,y)$,

$$\begin{aligned}\frac{2\pi B_{xq_n}(0,y)}{\mu_o I} &= \frac{2y}{n^2b^2+y^2} - \\ &\quad \frac{1}{b}\left[ctn^{-1}\left(\frac{2y}{b+2nb}\right) + ctn^{-1}\left(\frac{2y}{b-2nb}\right) + ctn^{-1}\left(\frac{2y}{b-2nb}\right) + ctn^{-1}\left(\frac{2y}{b+2nb}\right)\right] \\ &= \frac{2y}{n^2b^2+y^2} - \frac{2}{b}\left[ctn^{-1}\left(\frac{2y}{(2n+1)b}\right) - ctn^{-1}\left(\frac{2y}{(2n-1)b}\right)\right],\end{aligned} \tag{A6}$$

and the flux, ϕ_n, due to these two elements is

$$\begin{aligned}\frac{2\pi\phi_n}{\mu_o I} &= \ln\left(\frac{n^2+\Lambda^2}{n^2}\right) - (2n+1)\int_0^{2\Lambda/(2n+1)} ctn^{-1}\eta\, d\eta + (2n-1)\int_0^{2\Lambda/(2n-1)} ctn^{-1}\eta\, d\eta \\ &= \ln\left(\frac{n^2+\Lambda^2}{n^2}\right) - \frac{2n+1}{2}\ln\left(1+\frac{4\Lambda^2}{(2n+1)^2}\right) + \frac{2n-1}{2}\ln\left(1+\frac{4\Lambda^2}{(2n-1)^2}\right) \\ &\quad - 2\Lambda\left[ctn^{-1}\left(\frac{2\Lambda}{2n+1}\right) - ctn^{-1}\left(\frac{2\Lambda}{2n-1}\right)\right].\end{aligned} \tag{A7}$$

Now we algebraically rearrange the logarithmic terms in (A7) in such a way that they are grouped in like powers of n and the result is finite as Λ goes to infinity, and, which yields

$$\frac{2\pi\phi_n}{\mu_o I} = -n\ln\left(\frac{1+4\Lambda^2/(2n+1)^2}{1+4\Lambda^2/(2n-1)^2}\right)+\frac{1}{2}\ln\left(\frac{(n^2+\Lambda^2)(2n+1)^2}{n^2((2n+1)^2+4\Lambda^2)}\right)$$
$$+\frac{1}{2}\ln\left(\frac{(n^2+\Lambda^2)(2n-1)^2}{n^2((2n-1)^2+4\Lambda^2)}\right)-2\Lambda\left[ctn^{-1}\left(\frac{2\Lambda}{2n+1}\right)-ctn^{-1}\left(\frac{2\Lambda}{2n-1}\right)\right]. \quad \text{(A8)}$$

Letting Λ go to infinity,

$$\frac{2\pi\phi_n}{\mu_o I} = 2n\ln\left(\frac{(2n+1)}{(2n-1)}\right)+\ln\left(\frac{2n+1}{2n}\right)+\ln\left(\frac{2n-1}{2n}\right)-2$$
$$= 2n\ln\left(\frac{(2n+1)}{(2n-1)}\right)+\ln\left(1-\frac{1}{(2n)^2}\right)-2\,. \quad \text{(A9)}$$

The net flux due to ϕ_0 and all of the ϕ_n is thus[2]

$$\frac{2\pi\phi}{\mu_o I} \cong \ln\left(\frac{b}{2a}\right)-1+\sum_{n=1}^{\infty}\left[2n\ln\left(\frac{(2n+1)}{(2n-1)}\right)-2+\ln\left(1-\frac{1}{(2n)^2}\right)\right]$$
$$\cong \ln\left(\frac{b}{2a}\right)-1+1-\ln(2)+\ln(2\pi)=\ln\left(\frac{b}{2\pi a}\right). \quad \text{(A10)}$$

and the inductance per unit length of one wire of the coil is therefore

$$L'_{dis}(a/b)=\frac{dL_{dis}}{ds}\cong\frac{\mu_o}{2\pi}\ln\left(\frac{b}{2\pi a}\right). \quad \text{(A11)}$$

To calculate the contribution of discrete wires to the coil inductance, it is convenient to look at the coil in a coordinate system where the wire axes lie on a coordinate line. We will consider coils that lie in a plane (a surface of constant z). For our coils, in cylindrical coordinates the pitch *P* of the coil and the distance *b* separating the center of two adjacent windings are

$$P(r)=r\frac{d\theta}{dr}=kr,\quad b=\frac{2\pi r/N}{(1+P^2)^{1/2}}=\frac{2\pi r/N}{(1+(kr)^2)^{1/2}},\quad k=\Delta\theta/(b-a). \quad \text{(A12)}$$

Thus if we have *N* wires in a coil, they are spaced in angle $2\pi/N$ apart, and the inductance contributed by having discrete wires is

$$L_{dis} = \frac{1}{N}\int_{r_{inner}}^{r_{outer}} L'_{dis}\left(\frac{Na\left[1+P^2(r)\right]^{1/2}}{2\pi r}\right)\left[1+P^2(r)\right]^{1/2} dr$$
$$= \frac{\mu_o}{2\pi N}\int_{r_{inner}}^{r_{outer}} \ln\left(\frac{r}{Na\left[1+P^2(r)\right]^{1/2}}\right)\left[1+P^2(r)\right]^{1/2} dr\,. \qquad \text{(A13)}$$

The secondary coils are the most vulnerable to added inductance. For a 100-vane coil of 2 mm radius wires with $\pi/6$ wrap, 20 cm inner diameter, and 40 cm outer diameter, (A13) predicts an added inductance of 0.07 nH. That does not include the inductance for the inner and outer sections with radial wires. These can also be calculated with this formula using $k = 0.0$. For 5.0 cm radial vanes at each end of the above coil, another 0.07 nH is added.

1. H. B. Dwight, *Tables of Integrals and Other Mathematical Data*, 4th Ed., MacMillan, New York, 1961.
2. A. D. Wheelon, *Tables of Summable Series and Integrals Involving Bessel Functions*, Holden-Day, San Francisco, 1968.

Appendix B: ANALYTIC APPROXIMATIONS OF SELF AND MUTUAL INDUCTANCE AND A TABULATION OF ASSOCIATED PARAMETERS

The magnetic field from a particular configuration can be written as

$$\mathbf{B}(r,z) = \frac{\mu_o \Delta\theta\, I}{\delta}\mathbf{F}\left(\frac{r}{\delta},\frac{z}{\delta}\right), \tag{B1}$$

where **B** and **F** have only r and z components. $\delta = b - a$ is the difference between the inner and outer coil radii. For coil pitch $P(r)$ given by

$$P(r) = r\frac{d\theta}{dr} = \rho\frac{d\theta}{d\rho} = \Delta\theta\,\rho\, f(\rho), \text{ where } \rho = \frac{r}{\delta},$$

$$\frac{\mu_o IP}{2\pi r} = B_r(r,0^+) - B_r(r,0^-) = 2B_r(r,0^+) = -2B_r(r,0^-) \text{ or } F_r(r,0^\pm) = \frac{\pm f(\rho)}{4\pi} \tag{B2}$$

From Ampere's law

$$\int_{a/\delta}^{b/\delta} d\rho\, F_r(\rho,0^\pm) = \frac{\pm 1}{4\pi}\int_{a/\delta}^{b/\delta} f(\rho)\, d\rho = \frac{\pm 1}{4\pi} \;\Rightarrow\; \int_{a/\delta}^{b/\delta} f(\rho)\, d\rho = 1, \tag{B3}$$

where the first integral is infinitesimally above or below $z = 0$. For the special case where $f = 1$, $F_r(\rho,0^\pm) = \pm 1/(4\pi)$ for $a/\delta \le \rho \le b/\delta$ and zero for all other values of ρ.

The divergence of $\vec{F}$ is zero, therefore

$$\left[\frac{\partial F_z(\rho,\zeta)}{\partial\zeta}\right]_{\zeta=0^+} = -\left[\frac{1}{\rho}\left(\frac{\partial(\rho F_r(\rho,\zeta))}{\partial\zeta}\right)\right]_{\zeta=0^+} = -\frac{1}{4\pi\rho}\frac{d(\rho f)}{d\rho}, \text{ where } \zeta = \frac{z}{\delta}. \tag{B4}$$

Using our definition of the normalized inductance, $\mathcal{L} = L/(\delta\Delta\theta^2)$,

$$\mathcal{L} = \frac{1}{I\delta\Delta\theta^2}\left[\int_a^b dr B_z(r,0) r\left(\int_r^b \frac{d\theta}{dr}dr\right) + \Delta\theta\int_0^a dr B_z(r,0) r\right]$$

$$= \mu_o\left[\int_{a/\delta}^{b/\delta} d\rho\, F_z(\rho,0)\rho\left(\frac{1}{\Delta\theta}\int_\rho^{b/\delta}\frac{d\theta}{d\rho}d\rho\right) + \int_0^{a/\delta} d\rho\, F_z(\rho,0)\,\rho\right] \tag{B5}$$

The normalized mutual inductance, $\mathcal{M} = M/(\delta\Delta\theta^2)$, between two similar coils separated by a distance $\zeta = z/\delta$ can be expressed in a similar fashion, i.e.,

$$\mathcal{M}(\zeta) = \mu_o\left[\int_{a/\delta}^{b/\delta} d\rho\, F_z(\rho,\zeta)\rho\left(\frac{1}{\Delta\theta}\int_{\rho}^{b/\delta}\frac{d\theta}{d\rho}d\rho\right) + \int_{0}^{a/\delta} d\rho\, F_z(\rho,\zeta)\,\rho\right]. \tag{B6}$$

Approximating

$$F_z(\rho,\zeta) \cong F_z(\rho,0) + \left(\frac{\partial F_z(\rho,\zeta)}{\partial\zeta}\right)_{\zeta=0^+}|\zeta| = F_z(\rho,0) - \frac{1}{4\pi\rho}\frac{d(\rho f)}{d\rho}|\zeta|, \tag{B7}$$

combined with (B2), (B5), and (B6), yield

$$\mathcal{M}(\zeta) \cong \mathcal{L} - \kappa|\zeta|, \text{ where} \tag{B8}$$

$$\kappa = \frac{\mu_o}{4\pi}\left[\int_{a/\delta}^{b/\delta} d\rho\frac{d(\rho f)}{d\rho}\left(\int_{\rho}^{b/\delta} f\, d\rho\right) + \int_{0}^{a/\delta} d\rho\frac{d(\rho f)}{d\rho}\right]. \tag{B9}$$

Note that since f is discontinuous at $\rho = a/\delta$ and b/δ, the integrals involving its derivative in (B9) must be evaluated with care. To evaluate (B9) directly, distribution theory must be used to properly handle these discontinuities. Alternately, we can avoid the use of distributions for the integrals in (B9) containing derivatives of f if we first integrate them by parts, which gives

$$\kappa = \frac{\mu_o}{4\pi}\left[\int_{a/\delta}^{b/\delta} d\rho\,\rho f^2 - \int_{0}^{a/\delta} d\rho\, f + \frac{a}{\delta} f\left(\frac{a}{\delta}\right)\left(1 - \int_{a/\delta}^{b/\delta} d\rho\, f\right)\right] = \frac{\mu_o}{4\pi}\int_{a/\delta}^{b/\delta} d\rho\,\rho f^2\,. \tag{B10}$$

The final expression in (B10) was obtained by knowing that f is zero for $0 < \rho < a/\delta$ and the integral of f over the extent of the coil is unity.

For the case that $f = 1$, we find that

$$\kappa = \frac{\mu_o}{8\pi}\frac{b+a}{b-a} = 0.5\frac{b+a}{b-a}\ \text{nH/(cm rad}^2\text{)}. \tag{B11}$$

Using the Atheta 2D cylindrical magnetostatic code, values for $\mathcal{L}$ and $\mathcal{M}$ were computed. $\mathcal{M}$ was computed for intercoil spacing g/δ from 0 to 0.25. For each aspect ratio (b/a) and support structure separation (S/δ), the data for $\mathcal{M}$ was fit to a quadratic Taylor series, i.e.,

$$\mathcal{M}(g/\delta) \cong \mathcal{L}_0 - \kappa(g/\delta) + \kappa_2(g/\delta)^2, \tag{B12}$$

where $\mathcal{L}_0$ is the value of $\mathcal{L}$ computed for $g/\delta = 0$. Table B1 provides measured values of $\mathcal{L}_0$, using the coil figure function $f = 1$, for several combinations of b/a and S/δ. Similarly, Tables B2 and B3 provide the corresponding measured values if κ and κ_2, respectively. Note that the special case of no flux-excluding support structure is referred to as S/δ = *none*. Table B2 also includes an entry of the analytic value calculated using (B11), which is referred to as S/δ = *analytic*.

B1. Normalized inductances for various aspect ratios and support standoffs for *f* = 1.

$\mathcal{L}_0$ (nH/cm-rad^2)	$S/\delta = 0.05$	$S/\delta = 0.125$	$S/\delta = 0.25$	$S/\delta = 0.33$	S/δ = none
$b/a = 1.5$	1.046	1.185	1.348	1.427	1.926
$b/a = 2.0$	0.599	0.672	0.751	0.787	0.929
$b/a = 2.5$	0.447	0.496	0.546	0.567	0.637
$b/a = 3.0$	0.370	0.408	0.445	0.459	0.505
$b/a = 4.0$	0.293	0.319	0.342	0.350	0.379
$b/a = 5.0$	0.253	0.275	0.293	---	0.323

B2. Normalized mutual inductance linear fit coefficients for various aspect ratios and support standoffs for *f* = 1.

κ (nH/cm-rad^2)	$S/\delta = 0.05$	$S/\delta = 0.125$	$S/\delta = 0.25$	$S/\delta = 0.33$	S/δ = none	S/δ = analytic
$b/a = 1.5$	3.464	3.294	3.090	2.993	2.451	2.5
$b/a = 2.0$	1.992	1.884	1.752	1.695	1.470	1.5
$b/a = 2.5$	1.402	1.331	1.243	1.205	1.094	1.167
$b/a = 3.0$	1.250	1.176	1.092	1.060	0.979	1.0
$b/a = 4.0$	0.908	0.868	0.828	0.816	0.781	0.833
$b/a = 5.0$	0.885	0.834	0.788	---	0.733	0.75

B3. Normalized mutual inductance quadratic fit coefficients for various aspect ratios and support standoffs for *f* = 1.

κ_2 (nH/cm-rad^2)	$S/\delta = 0.05$	$S/\delta = 0.125$	$S/\delta = 0.25$	$S/\delta = 0.33$	S/δ = none
$b/a = 1.5$	5.530	4.541	3.671	3.346	2.173
$b/a = 2.0$	3.14	2.572	2.053	1.878	1.363
$b/a = 2.5$	2.029	1.652	1.313	1.200	0.945
$b/a = 3.0$	1.954	1.589	1.277	1.177	0.980
$b/a = 4.0$	1.212	1.003	0.848	0.809	0.745
$b/a = 5.0$	1.375	1.126	0.945	---	0.799

Equation (B5) gives an integral expression for $\mathcal{L} = L/(\delta\Delta\theta^2)$. The function $F_z(\rho,0)$ itself involves elliptic integrals, so there is no analytical expression for $\mathcal{L}$. There is, however, an approximate formula for the $\mathcal{L}$ which contains a single variable that varies slowly with geometry. Consider a toroidal loop with major radius *R*, and minor radius *r*. The total flux through the toroid is ϕ, and the current in the toroid is *i*. The inductance, L_T, can then be written as

$$L_T = \frac{\phi}{i} = 2\pi R \frac{\mu_o}{2\pi} \ln\left(\frac{\sigma R}{r}\right) = \mu_o R \ln\left(\frac{\sigma R}{r}\right), \tag{B13}$$

where σ is of order one. This expression comes from approximating the loop by a coaxial line of length $2\pi R$ with inner and outer radii of r and σR, respectively.

We would expect (B13) to be approximately correct for a washer-shaped transformer coil using the following relationships:

$$R = \frac{b+a}{2}, \quad r = \frac{b-a}{2}, \quad i = \frac{\Delta\theta}{2\pi} I, \quad \Phi = \frac{\Delta\theta}{2\pi}\phi, \text{ and where } L = \frac{\Phi}{I}, \tag{B14}$$

at least when $(b-a)/(b+a) << 1$. Then

$$\frac{(2\pi)^2 \Phi}{\Delta\theta^2 I} = \frac{(2\pi)^2 L}{\Delta\theta^2} = \frac{\phi}{i} = \mu_o \frac{b+a}{2} \ln\left(\frac{\sigma(b+a)}{b-a}\right), \text{ which leads to} \tag{B15}$$

$$\mathcal{L} = \frac{L}{(b-a)\Delta\theta^2} = \frac{\mu_o}{8\pi^2} \frac{b+a}{b-a} \ln\left(\frac{\sigma(b+a)}{b-a}\right). \tag{B16}$$

Table B4 provides measured values of σ, using the coil figure function $f = 1$, for several combinations of b/a and S/δ. These values were obtained by substituting $\mathcal{L}$ from Table B1 into (B16) and solving for σ. Note that σ varies slowly with the coil aspect ratio b/a, and $\mathcal{L}$ varies only as the logarithm of σ. As one would expect, the presence of flux-excluding supports does have a significant effect on this parameter.

Table B4. Normalized inductance σ parameter for various aspect ratios and support standoffs for $f = 1$.

σ	$S/\delta = 0.05$	$S/\delta = 0.125$	$S/\delta = 0.25$	$S/\delta = 0.33$	S/δ = none
$b/a = 1.5$	0.745	0.887	1.088	1.202	2.249
$b/a = 2.0$	1.169	1.361	1.606	1.878	2.333
$b/a = 2.5$	1.429	1.630	1.865	1.973	2.381
$b/a = 3.0$	1.599	1.803	2.023	2.114	2.445
$b/a = 4.0$	1.808	1.995	2.178	2.245	2.507
$b/a = 5.0$	1.927	2.107	2.274	---	2.576

Using (B11), (B12), and (B16), and neglecting the κ_2 term in (B12), we can derive an approximate expression for the ratio of mutual inductance to self inductance (which is the square root of the transformer coupling efficiency η):

$$\frac{\mathcal{M}}{\mathcal{L}} = 1 - \frac{\kappa}{\mathcal{L}} \frac{g}{b-a} = 1 - \frac{\pi}{\ln[\sigma(b+a)/(b-a)]} \frac{g}{b-a}. \tag{B17}$$

Appendix C: CIRCUIT MODELS FOR SYSTEMS AND LOADS OF INTEREST

This appendix derives the differential equations that describe the various systems and loads for this report. In addition, details of their numerical solution are provided.

C.1. Transformer Circuits of Interest

C.1.1. The Basic Transformer with a Purely Inductive Load

Consider the circuit diagram shown in Fig. 11, which consists of two distinct loops. The loop on the left, which we will call the *primary* loop, includes the Thévenin-equivalent voltage source characterized by V_0 and Z_0. The loop on the right, which includes a purely inductive, possibly time-dependent, load $L(t)$, will be referred to as the *secondary* loop. We define I_p and I_s to be the currents in the primary and secondary loops, respectively, which are considered positive when flowing in the clockwise direction. Note that for the basic transformer, these currents are coupled only through the mutual inductance M.

Although we use $L(t)$ in the equations throughout the remainder of this Appendix, load inductances, when time dependent, are modeled as functions of a shell radius that varies in time. Consequently, time derivatives of $L(t)$ can always be written as $dL/dt = (dL/dr)(dr/dt)$.

The total magnetic flux in the two loops, denoted Φ_p and Φ_s, are

$$\Phi_p = L_o I_p + \left(L_p I_p - M I_s\right), \text{ and} \tag{C1}$$

$$\Phi_s = \left(L_s I_s - M I_p\right) + L(t) I_s . \tag{C2}$$

The total flux in the closed secondary loop must be zero, which when combined with (C2), leads to

$$\frac{I_s}{I_p} = \frac{M}{L_s + L(t)} \equiv R, \tag{C3}$$

where R is the current multiplication ratio of the transformer. Note that for the basic transformer, the short-circuit (i.e., $L(t) = 0$) current multiplication ratio, R_{SC}, is simply M/L_s, and that R decreases from that value as the load inductance increases. If (C3) is used to replace I_s in (C1), we obtain

$$\Phi_p = L_{eff} I_p, \text{ where } \; L_{eff}(t) = L_o + L_p - \frac{M^2}{L_s + L(t)} = L_o + L_p\left(1-\eta\right) + \frac{M^2 L(t)}{L_s\left[L_s + L(t)\right]}, \tag{C4}$$

and $\eta = M^2 / L_p L_s$ is the coupling efficiency of the transformer. The rightmost expression for L_{eff} in (C4) separates the dependence on the load inductance $L(t)$ to a single term which vanishes when $L(t)$ is zero. In the primary loop, the time derivative of the loop's flux must equal the voltage drop across the Thévenin-equivalent source, which yields the differential equation for the basic transformer,

$$\frac{d\Phi_p}{dt} = \frac{d(L_{eff} I)}{dt} = 2v_0(t) + Z_0 I\,, \tag{C5}$$

where $I = I_p$ is the current driven by the Thévenin-equivalent source. The secondary current I_s can be obtained from I using (C3).

C.1.2. The Auto Transformer Circuit with a Purely Inductive Load

The auto transformer's circuit (see Fig. 12) is similar to the basic transformer in that it has primary and secondary loops, each with clockwise currents I_p and I_s. However, both loops share the flux in the secondary inductor of the transformer, and the current through the secondary inductor is the difference of the two loop currents, i.e., $I_2 = I_p - I_s$. In this case, the total flux in each of the loops is

$$\Phi_p = L_o I_p + \left[L_p I_p - M\left(I_s - I_p\right)\right] + \left[M I_p - L_s\left(I_s - I_p\right)\right], \text{ and} \tag{C6}$$

$$\Phi_s = \left[L_s\left(I_s - I_p\right) - M I_p\right] + L(t) I_s\,. \tag{C7}$$

Setting (C7) to zero, an expression for the transformer's current multiplication ratio is obtained:

$$\frac{I_s}{I_p} = \frac{L_s + M}{L_s + L(t)} \equiv R\,. \tag{C8}$$

Note that the auto transformer has higher current multiplication than the basic transformer. Substituting (C7) into (C6) yields and effective inductance for the auto transformer,

$$L_{eff}(t) = L_o + L_p - \frac{M^2 - (2M + L_s)L(t)}{L_s + L(t)} = L_o + L_p(1-\eta) + \frac{(M + L_s)^2}{L_s\left(L_s + L(t)\right)} L(t)\,. \tag{C9}$$

The differential equation for the auto transformer, of course, is the same as that for the basic transformer (C5), but I_s is now obtained from I using (C8).

C.1.3. Transformer Systems with a Resistor in the Load Circuit

With the addition of a series resistor in the load circuit, it is no longer possible to algebraically eliminate one of the system's two state variables (I_p and I_s) to arrive at a single first-order differential equation for the circuit. One is now forced to solve a system of two first-

order equations for the two circuit loops, along with any other equations that might arise from the model for a complex load, such as the PRS. The equations are obtained by setting the time derivatives of the flux in each loop to the voltage drop across any other elements of that loop. This results in the following pair of differential equations:

$$L_{00}\frac{dI_p}{dt} - L_{10}\frac{dI_s}{dt} = 2v_0(t) - Z_0 I_p(t) \text{ and}$$
$$L_{10}\frac{dI_p}{dt} - L_{11}(t)\frac{dI_s}{dt} = \left[Z_i + \dot{L}(t)\right]I_s(t), \tag{C10}$$

where Z_i is the resistance in the load circuit and $\dot{L}(t) \equiv \frac{dL}{dt}$.

For both the basic and auto transformer,

$$L_{11}(t) = L_s + L(t). \tag{C11}$$

For the basic transformer of Section C.1.1 above, the other coefficient for (C10) are

$$L_{00} = L_o + L_p \text{ and } L_{10} = M, \tag{C12}$$

while for the auto transformer, they are

$$L_{00} = L_o + L_p + L_s + 2M \text{ and } L_{10} = L_s + M. \tag{C13}$$

If the series resistance is small, i.e., $I_s Z << d[L(t)I]/dt$, then the expressions for the effective inductance L_{eff} and the current multiplication ratio R given in Sections C.1.1 and C.1.2 above, although not exact, will be very good estimates for the inductance seen by the source and the current amplification, respectively. For the case of the PRS load model with an ohmically-heated internal gas, this will always be the case.

C.2. Circuit Model for Convolute Current Adder

The circuit model for the convolute current adder, shown schematically in Fig. 13, is complicated by the presence of the nonlinear Z_{loss} element as described in Section 2.2.4 above. Specifically, the voltage drop across the loss element is related to its input and output currents by the relationship

$$\frac{v_1}{\sqrt{I_0^2 - I_1^2}} = f_\ell(t)\, Z_{loss}, \text{ where} \tag{C14}$$

$$f_\ell(t) = \begin{cases} 1, & \text{for } t < t_{thresh} \\ e^{-(t-t_{thresh})/\tau_\ell}, & \text{for } t > t_{thresh} \end{cases} \tag{C15}$$

where v_1 is the voltage drop across the Z_{loss} element, τ_ℓ is a specified decay time for Z_{loss}, and t_{thresh} is the time at which the energy dissipated in the Z_{loss} element reaches a specified value E_{thresh}, i.e.,

$$E_{loss}(t_{thresh}) = E_{thresh}, \text{ where } E_{loss}(t) \equiv \int_0^t v_1\left[I_0(t') - I_1(t')\right]dt' \tag{C16}$$

The parameters τ_ℓ and E_{thresh} are chosen to match experimental data.

Two first-order differential equations that describe this circuit are obtained by choosing two loops over which the total voltage is constrained to be zero. For this case, it is simplest to select the left-most loop and the outer loop (see Fig. 13), which leads to the following equations:

$$\begin{aligned} &L_0 \frac{dI_0}{dt} = 2v_0(t) - Z_0 I_0(t) - Z_{loss}(t)\left[I_0^2(t) - I_1^2(t)\right]^{1/2} \text{ and} \\ &L_0 \frac{dI_0}{dt} + \left[L_1 + L(t)\right]\frac{dI_1}{dt} = 2v_0(t) - Z_0 I_0(t) - \left[Z_i + \dot{L}(t)\right]I_1(t). \end{aligned} \tag{C17}$$

C.3. Circuit Models for PRS Loads

For our idealized model of a PRS load of height h, mass m, initial radius r_i, and return current radius r_o, we assume that the mass is concentrated in an infinitesimally thin shell with radius $r(t)$, and that the forces acting upon it are uniform both axially and azimuthally. Since all of the circuit models derived in the previous sections require both the inductance of the load and its time derivative, and these quantities depend on time only through $r(t)$, it is convenient to cast the $\partial^2 r/dt^2$ needed for the acceleration of the load's mass into time derivatives of the load inductance. With that in mind, we introduce a normalized load inductance χ, by

$$L(t) = L_N \chi(t), \text{ where } \chi(t) = \ln\left(r_o / r(t)\right) \text{ and } L_N = \frac{\mu_o h}{2\pi}. \tag{C18}$$

It is easy to show that

$$\ddot{r} = -r\left(\ddot{\chi} - \dot{\chi}^2\right), \tag{C19}$$

where the "dot" notation indicates the usual one or two time derivatives. Substituting into Newton's second law, we obtain

$$-mr(t)\left(\ddot{\chi}-\dot{\chi}^2\right)=\frac{I_L^2}{2}\frac{dL(t)}{dr}+2\pi hr(t)P_M(t)\,. \tag{C20}$$

The first term on the right-hand side of (C20) is force applied the load by the magnetic field, and the second term is an opposing force supplied by an as yet unspecified pressure. Using (C18) to express r and dL/dr in terms of χ, (C20) becomes

$$mr_o^2\left(\ddot{\chi}-\dot{\chi}^2\right)=\frac{L_N I_L^2}{2}e^{2\chi}-2\pi hr_o^2P_M(t)\,. \tag{C21}$$

With the introduction of a new state variable ρ, (C21) can be expressed as two first-order equations, i.e.,

$$\begin{aligned}\dot{\chi}&=\rho\,,\\ \dot{\rho}&=\rho^2+\frac{I_L^2}{2Q_0^2}e^{2\chi}-\frac{2\pi h}{m}P_M(t)\,.\end{aligned} \tag{C22}$$

where $Q_0^2=mr_o^2/L_N$. Note that $\dot{L}(t)$, which is needed (C5), (C10), and (C17), is simply $L_N\rho$.

C.3.1. Minimum Radius Model

First consider the simplest model for the force that decelerates the PRS load as it approaches the axis, which is simply to ignore it and stop the calculation when the load shell reaches a specified inner radius. In that case the last term in the $\dot{\rho}$ equation of (C22) vanishes. The two equations in (C22) are then solved simultaneously with the one or more first-order equations from the circuit model of interest.

C.3.2. Adiabatic Compression of Gas Fill

For the next simplest model that we will examine, it is assumed that the decelerating force is supplied by a ideal gas within the load shell that is adiabatically compressed as the shell is accelerated toward the axis. The initial pressure of the gas, P_i, is presumably chosen to best match experimental observations of these loads. For an monatomic ideal gas undergoing adiabatic compression, PV^γ is a constant, where P and V are the pressure and volume of the gas, respectively, and $\gamma=C_p/C_v=5/3$ is the specific heat ratio. For this case, P_M in (C22) becomes

$$P_M(t)=P_i\frac{V_i^\gamma}{V(t)^\gamma}=P_i\left(\frac{r_i^2}{r(t)^2}\right)^\gamma=P_i\left(\frac{r_i}{r_o}\right)^{2\gamma}e^{2\chi\gamma}\,. \tag{C23}$$

C.3.3. Low Density Gas Fill with Compression and External Heating

For the last model that we will examine, it is assumed that the decelerating force is supplied by a very low-density (i.e., its initial pressure is negligible) ideal gas that is ohmically heated with the load current. The resistance of the gas is chosen to best mimic the behavior of actual z-pinches as they approach stagnation. The gas has an internal energy U, initially zero, and pressure $P = (\gamma - 1)U/V$. The change in the internal energy in time dt is $dU = dQ - PdV$, where dQ is the energy dissipated heating the gas. For this case, P_M in (C22) becomes

$$P_M(t) = \frac{(\gamma-1)U(t)}{V(t)} = \frac{(\gamma-1)U(t)}{\pi h r_o^2} e^{2\chi}, \tag{C24}$$

where $V(t)$ is the time-dependent volume of the load. Note that for this case U becomes another state variable, with the associated new differential equation

$$\frac{dU}{dt} = \frac{dQ}{dt} - P\frac{dV}{dr}\frac{dr}{dt} = Z_i I_L^2 + 2(\gamma-1)\rho U . \tag{C25}$$

Now (C22), (C24), and (C25), combined with either (C10) or (C17), provide a system of five first-order equations that describe the behavior of the circuit.

C.4. Circuit Model for Tesla Experiment

The output current of Tesla flows radially inward into the vacuum chamber in two transmission lines comprised of three disks. The outer two disks are positive and the inner disk is negative, so the two transmission lines have electric and magnetic fields that are in opposite directions. The transformer was designed to add the currents of the two inputs without a convolute, and then to multiply the sum of the two currents by some factor.

A schematic of the Tesla transformer is shown in Fig. 30. The figure shows a transformer with four coils, and all will be included in the circuit equations, but in the experiment the fourth "coil" consisted of radial vanes, so that its self inductance, and the mutual inductance between it and all the other coils were zero. Here we consider the two inputs to be in parallel, so $\Phi_p = \Phi_a = \Phi_b$, but in the circuit modeling and the experiment there was a small difference in the inductance of the two feeds. The magnetic flux in each of the four coils is given by

$$\begin{aligned}
\Phi_1 &= (L_1 + M_{13})I_a + (M_{14} + M_{12})I_b - (M_{13} - M_{14})I_s \\
\Phi_2 &= (M_{23} + M_{12})I_a + (L_2 + M_{24})I_b + (M_{24} - M_{23})I_s \\
\Phi_3 &= (L_3 + M_{13})I_a + (M_{34} + M_{23})I_b - (L_3 - M_{34})I_s \\
\Phi_4 &= (M_{14} + M_{34})I_a + (L_4 + M_{24})I_b + (L_4 - M_{34})I_s
\end{aligned} \tag{C26}$$

where M_{ij} is the mutual inductance between L_i and L_j. Referring to Fig. 30, we can obtain expressions for the flux in each loop, i.e.,

$$\begin{aligned}\Phi_a &= \Phi_1 + \Phi_3 = K_1 I_a + K_o I_b - K_3 I_s \\ \Phi_b &= \Phi_2 + \Phi_4 = K_o I_a + K_2 I_b + K_4 I_s \\ \Phi_s &= \Phi_3 - \Phi_4 = K_3 I_a - K_4 I_b - K_s I_s\end{aligned} \tag{C27}$$

where

$$\begin{aligned}K_o &= M_{12} + M_{23} + M_{34} + M_{14}, \quad K_s = L_3 + L_4 - 2M_{34} \\ K_1 &= L_1 + L_3 + 2M_{13}, \quad K_2 = L_2 + L_4 + 2M_{24} \\ K_3 &= L_3 + M_{13} - M_{14} - M_{34}, \quad K_4 = L_4 + M_{24} - M_{23} - M_{34}.\end{aligned} \tag{C28}$$

Using $\Phi_p = \Phi_a = \Phi_b$, $I_p \equiv I_a + I_b$, and $\Delta I \equiv I_a - I_b$, we can derive the following relationships:

$$\Phi_a - \Phi_b = 0 \;\Rightarrow\; \frac{K_1 - K_2}{2} I_p + \frac{K_1 + K_2 - 2K_o}{2} \Delta I = (K_3 + K_4) I_s, \tag{C29}$$

$$\Phi_p = \frac{\Phi_a + \Phi_b}{2} = \frac{K_1 + K_2 + 2K_o}{4} I_p + \frac{K_1 - K_2}{4} \Delta I - K_s I_s, \text{ and} \tag{C30}$$

$$\Phi_s = \frac{K_3 - K_4}{2} I_p + \frac{K_3 + K_4}{2} \Delta I - K_s I_s. \tag{C31}$$

If we consider using this circuit to drive purely inductive loads, we can equate Φ_s with $L_s I_s$, where L_s includes any B_θ inductance in the secondary circuit in addition to the load inductance connected to the circuit's output terminals. We can determine an effective inductance by algebraic manipulation of (C29-C31). Combining (C29) and (C31) with the constraint that $\Phi_s = L_s I_s$, we find that

$$\frac{I_s}{I_p} = -\frac{K_1 - K_2 - \alpha(K_3 - K_4)}{2\left[K_3 + K_4 - \alpha(K_s + L_s)\right]} \equiv \beta, \tag{C32}$$

where $\alpha = \left(K_1 + K_2 - 2K_0\right)/\left(K_3 + K_4\right)$. Combining (C31) and (C32) yields

$$\frac{\Delta I}{I_p} = -\frac{2\left(K_s + L_s\right)\beta - \left(K_3 - K_4\right)}{K_3 + K_4} \equiv \gamma. \tag{C33}$$

Finally, combining (C30), (C32), and (C33), we obtain the effective inductance

$$\frac{\Phi_p}{I_p} \equiv L_{eff} = \frac{K_1 + K_2 + 2K_0 + \left(K_1 - K_2\right)\gamma}{4} - \frac{\left(K_3 - K_4\right)}{2}\beta. \tag{C34}$$

Combined with (C5), we have a first-order differential equation that can be integrated to find $I_p(t)$. The other currents can be determined using (C32) and (C33).

C.5. Numerical Solution Techniques

We now discuss how the governing differential equations for a given circuit model are discretized and integrated numerically. We represent time in discrete units, with a timestep Δt. We adopt the notation that X_k represents $X(k\Delta t)$, where X is any one of the system's state variables. For the circuit models described previously in this appendix, we a have one or two current state variables. If the load inductance is time-dependent, two more state variables for the normalized inductance χ and its time derivative ρ, and possibly another for the internal energy of the load (U). To simplify issues of time-centering the integration over a timestep, it is convenient to temporally locate all currents, χ, and U at integral multiples of Δt, and ρ midway between (at the "half" timestep). We will then center all differences using linear interpolation if necessary.

If we assume that ρ is known at the half-timestep "k-½" (i.e., $\rho_{k\text{-}1/2}$), and that the currents, χ, and U are known at timestep "k", then we need to determine how to advance each of these quantities one timestep to temporal steps "k+½" and "k+1", respectively. We will describe the details for the two circuits described in Sections C.1.3 and C.2, using the PRS load model described in Section C.3.3. Other circuit/load combinations are less complex, and their integration would follow a similar approach.

C.5.1. Auto Transformer with Low Density Gas Fill PRS Model

Since at the kth timestep, ρ has the "oldest" value at k-½, we will advance it first. If we integrate the $\dot{\rho}$ equation of (C22) from (k-½)Δt to (k+½)Δt, and assume that the integrand can be approximated by its value midway in time through the integration, we obtain

$$\Delta\rho \equiv \rho_{k+1/2} - \rho_{k-1/2} = +\Delta t\left\{\rho_k^2 + \Omega^2(\chi_k, I_{sk}, U_k)\right\}, \tag{C35}$$

where

$$\Omega^2(\chi, I_L, U) = \frac{I_L^2}{2Q_0^2}e^{2\chi} - \frac{2(\gamma-1)U(t)}{mr_o^2}e^{2\chi}. \tag{C36}$$

Integrating the remaining equation of (C22) from $k\Delta t$ to (k+1)Δt, we obtain

$$\chi_{k+1} = \chi_k + \Delta t\rho_{k+1/2}. \tag{C37}$$

Similarly, (C10), with the substitution that $I_s = I_L$, becomes

$$L_{00}\Delta I_p - L_{10}\Delta I_L = 2\Delta t v_{k+1/2} - Z_0\Delta t I_{p_{k+1/2}} \text{ and}$$

$$L_{10}\Delta I_p - \left[L_2 + L_N \chi_{k+1/2}\right]\Delta I_L = I_{Lk+1/2}\left[Z_i + L_N \rho_{k+1/2}\right]\Delta t\,, \tag{C38}$$

which must be solved simultaneously. Here, $\Delta I_p \equiv I_{p_{k+1}} - I_{p_k}$ and $\Delta I \equiv I_{Lk+1} - I_{Lk}$. Note that the value of $\chi_{k+1/2}$ needed in (C38) is just the mean of χ_k and χ_{k+1} (using Eq.C37), i.e.,

$$\chi_{k+1/2} = \frac{\chi_k + \chi_{k+1}}{2}. \tag{C39}$$

Finally, (C25) becomes

$$\Delta U \equiv U_{k+1} - U_k = \left[ZI^2_{Lk+1/2} + 2(\gamma - 1)\rho_{k+1/2}U_{k+1/2}\right]\Delta t\,. \tag{C40}$$

Note that once (C38) has been solved for ΔI_s, the half-time-step current value needed in (C40) is simply $I_{Lk} + \Delta I_L/2$.

Although our choice of time location for the system's state variables have dealt with several of the time-centering issues, note that (C35), both of (C38), and (C40) have the complication that a variable is needed at a time index that does not fall on our chosen discretization (ρ_k, $I_{p_{k+1/2}}$, $I_{Lk+1/2}$, and $U_{k+1/2}$). We consequently need to approximate these values with some combination of the surrounding discrete values that we do have. We will chose to make this approximation with a weighted linear combination, with a weighting factor that reflects the implicitness of the approximation. For example, we will approximate $X_{k+1/2}$ by $X_k + \beta\Delta X$, where $0 \le \beta \le 1$, and X is any one of our state variables. When $\beta = 0$, the integration is explicit; when $\beta = 1$, it becomes fully implicit. When $\beta = ½$, the differences are centered. With this approximation, (C38) becomes

$$\begin{aligned} &\left(L_{00} + \beta Z_0 \Delta t\right)\Delta I_p - L_{10}\Delta I_L = \left(2v_{k+1/2} - Z_0 I_{p_k}\right)\Delta t \text{ and} \\ &L_{10}\Delta I_p - \left[L_2 + L_N \chi_{k+1/2} + \beta\left(Z_i + L_N \rho_{k+1/2}\right)\Delta t\right]\Delta I_L = I_{Lk}\left[Z_i + L_N \rho_{k+1/2}\right]\Delta t\,. \end{aligned} \tag{C41}$$

This pair of linear equations can now be solved simultaneously for ΔI_p and ΔI_L, from which values of $I_{p_{k+1}}$ and I_{Lk+1} can be determined.

Similarly, we can approximate (C40) by

$$\Delta U = \frac{\left[ZI^2_{Lk+1/2} + 2(\gamma - 1)\rho_{k+1/2}U_k\right]\Delta t}{1 - 2\beta(\gamma - 1)\rho_{k+1/2}\Delta t},\ I_{Lk+1/2} = I_{Lk} + \Delta I_s/2\,. \tag{C42}$$

We adopt a similar approach to approximating ρ_k in (C35), i.e.,

$$\Delta\rho_k = \Delta t\left[\left(\rho_{k-1/2} + \alpha\,\Delta\rho_k\right)^2 + \Omega^2(\chi_k, I_{Lk}, U_k)\right], \tag{C43}$$

where $0 \le \alpha \le 1$. Note that this expression is complicated by the fact that ρ_k appears as the square in (C35). Rearranging terms in (C43), we obtain a quadratic equation for $\Delta\rho_k$,

$$\alpha^2\Delta t\Delta\rho_k^2 - \left(1 - 2\alpha\Delta t\rho_{k-1/2}\right)\Delta\rho_k + \Delta t\left(\rho_{k-1/2}^2 + \Omega_k^2\right) = 0, \tag{C44}$$

where $\Omega_k^2 \equiv \Omega^2(\chi_k, I_{Lk}, U_k)$. The solution of (C44) is

$$\Delta\rho_k = \frac{2\left(\rho_{k-1/2}^2 + \Omega_k^2\right)\Delta t}{1 - 2\alpha\Delta t\rho_{k-1/2} + \sqrt{1 - 4\alpha\Delta t\rho_{k-1/2} - 4\alpha^2\Delta t^2\Omega_k^2}}, \tag{C45}$$

where we have chosen the sign of the square root so that the correct value is obtained in the fully explicit limit ($\alpha = 0$). If we linearize (C44) by discarding its first term (which is third order in Δt), we obtain the simpler result

$$\Delta\rho_k \cong \frac{\left(\rho_{k-1/2}^2 + \Omega_k^2\right)\Delta t}{1 - 2\alpha\Delta t\rho_{k-1/2}}, \tag{C46}$$

which should be quite accurate if Δt is sufficiently small.

For initial conditions, we will assume that $\rho_{-1/2} = I_{p_0} = I_{L0} = U_0 = 0$ and $\chi_0 = \ln(r_o/r_i)$. Then (C45), (C37), (C41), and (C42) are applied, in that order, for $k = 0$. This process is repeated for successive values of k until the desired final time ($N\Delta t$) is reached. In our implementations to date, we have successfully used exactly-centered differences ($\alpha = \beta = ½$).

C.5.2. Convolute System with Low Density Gas Fill PRS Model

For the convolute system, shown schematically in Fig. 13, much of the analysis of the previous section (C.5.1) can be used. With the substitution that I_1 of Fig. 13 is the load current I_L, (C45), (C37), and (C42) can be used to update the non-current state variables. We simply need to replace (C41) with an equivalent single-step integration of (C17), which is specific to the convolute model. Further, all the state variables are temporally located at the same locations as in the previous section. Integrating the two equations of (C17) from $k\Delta t$ to $(k+1)\Delta t$, and setting $I_1 = I_L$, we obtain

$$L_0\Delta I_0 = \left[2v_{0k+1/2} - Z_0 I_{0k+1/2} - v_{1k+1/2}\right]\Delta t \quad \text{and} \tag{C47}$$

$$L_0\Delta I_0 + \left[L_1 + L_N\chi_{k+1/2}\right]\Delta I_L = \left\{2v_{0k+1/2} - Z_0 I_{0k+1/2} - I_{Lk+1/2}\left[Z_i + L_N\rho_{k+1/2}\right]\right\}\Delta t\,,$$

where

$$v_{1m} \equiv Z_{loss}\, f_\ell(m\Delta t)\left[I_0^2(m\Delta t) - I_L^2(m\Delta t)\right]^{1/2}. \tag{C48}$$

Since v_1 is a function of the two current state variables (I_0 and I_L), it is also temporally located at integral multiples of the timestep. Consequently, v_1, I_0, and I_L are needed in (C47) at a time index that does not fall on our discretization and will require a weighted average of their two bounding values as described in the previous section. First we handle the explicit references to the currents in the right-hand sides of the two equations in (C47), leading to

$$\begin{aligned}
&\left[L_0 + \beta Z_0\Delta t\right]\Delta I_0 = \left[2v_{0k+1/2} - Z_0 I_{0k} - v_{1k+1/2}\right]\Delta t \text{ and} \\
&\left[L_0 + \beta Z_0\Delta t\right]\Delta I_0 + \left[L_1 + L_N\chi_{k+1/2} + \beta\Psi_{k+1/2}\Delta t\right]\Delta I_L = \left[2v_{0k+1/2} - Z_0 I_{0k} - I_{Lk}\Psi_{k+1/2}\right]\Delta t\,,
\end{aligned} \tag{C49}$$

where

$$\Psi_{k+1/2} \equiv Z_i + L_N\rho_{k+1/2}\,. \tag{C50}$$

Now all that is left is to obtain an expression for $v_{1k+1/2}$ that is a function of I_{0k}, I_{Lk}, ΔI_0, and ΔI_L. Replacing the currents in (C48) for $m = k+½$ with their extrapolated values, we obtain

$$\begin{aligned}
v_{1k+1/2} &= Z_{loss}\, f_{\ell k+1/2}\left[\left(I_{0k} + \beta\Delta I_0\right)^2 - \left(I_{Lk} + \beta\Delta I_L\right)^2\right]^{1/2} \\
&= Z_{loss}\, f_{\ell k+1/2}\left[\mathcal{I}_k^2 + 2\beta\left(I_{0k}\Delta I_0 - I_{Lk}\Delta I_L\right) + \beta^2\left(\{\Delta I_0\}^2 - \{\Delta I_L\}^2\right)\right]^{1/2}
\end{aligned} \tag{C51}$$

where $\mathcal{I}_k^2 = I_{0k}^2 - I_{Lk}^2$.

If the $\mathcal{I}_k^2$ is factored out of the square root term in (C51), the remaining square root expanded in a Taylor series about one, and the second-order and higher terms in ΔI_0 and ΔI_L discarded, we obtain the desired expression,

$$v_{1k+1/2} = Z_{\ell k+1/2}\left[\mathcal{I}_k + \frac{\beta}{\mathcal{I}_k}\left(I_{0k}\Delta I_0 - I_{Lk}\Delta I_L\right)\right],\quad Z_{\ell k+1/2} = Z_{loss}\, f_{\ell k+1/2}\,. \tag{C52}$$

Substituting (C52) into (C49), we finally obtain

$$\left[L_0+\beta\Delta t\left(Z_0+Z_{\ell k+1/2}\frac{I_{0k}}{\mathcal{I}_k}\right)\right]\Delta I_0+\left[\beta\Delta t Z_{\ell k+1/2}\frac{I_{Lk}}{\mathcal{I}_k}\right]\Delta I_L=\left[2v_{0k+1/2}-Z_0I_{0k}-Z_{\ell k+1/2}\mathcal{I}_k\right]\Delta t$$

$$\left[L_0+\beta Z_0\Delta t\right]\Delta I_0+\left[L_1+L_N\chi_{k+1/2}+\beta\Psi_{k+1/2}\Delta t\right]\Delta I_L=\left[2v_{0k+1/2}-Z_0I_{0k}-I_{Lk}\Psi_{k+1/2}\right]\Delta t\,. \tag{C53}$$

In order to determine the value of $f_{\ell k+1/2}$ needed in (C53), we need to evaluate E_{loss} from (C16) in order to determine τ_ℓ. E_{loss} can be computed from one timestep to the next using

$$\Delta E_{loss}\equiv E_{loss\,k+1/2}-E_{loss\,k-1/2}+v_{1k}\left(I_{0k}-I_{Lk}\right). \tag{C54}$$

On the first timestep where $E_{loss\,k+1/2}$ exceeds the specified value of E_{thresh}, denoted by k_0, the value of τ_ℓ can be determined via linear interpolation, i.e.,

$$\tau_\ell=\left[k_0+\frac{E_{thresh}-E_{loss\,k_0}}{\Delta E_{loss}}\right]\Delta t\text{ , where }E_{loss\,k}=E_{loss\,k-1/2}+\frac{\Delta E_{loss}}{2}. \tag{C55}$$

For initial conditions, we will assume that $\rho_{-1/2}=E_{loss-1/2}=I_{00}=I_{L0}=U_0=0$ and $\chi_0=\ln(r_o/r_i)$. Then (C45), (C51), (C37), (C53), and (C42) are applied, in that order, for $k = 0$. This process is repeated for successive values of k until the desired final time ($N\Delta t$) is reached.

Appendix D: QUICKSILVER 2D COIL MODEL

Although the individual coil windings in a transformer are strictly 3D, the coils in aggregate can be modeled as a "solid" conductor with infinite conductivity parallel to the windings, and with zero conductivity perpendicular to the windings. In general, the pitch of the windings, and consequently the direction of infinite conductivity, will vary as a function of radial position. Note that this approach will not model any effects related to winding radii or spacing, which would require full 3D treatment. An early version[1] of this model had been implemented previously in Sandia's TwoQuick[2] 2D electromagnetic PIC code, but did not have any provisions for handling interactions between the coils and electrons. For this reason, and because TwoQuick lacked several other features that were important to our modeling effort for this type of system, we added an enhanced version of the original algorithm. The remainder of this Appendix provides a general description of the algorithm as implemented in Quicksilver.

D.1. EM model for 2D coil

To simplify the derivation of this model, we will assume that the coordinate system is cylindrical, the problem is independent of the azimuthal coordinate θ, and that the coil lies in a ξ-θ coordinate surface, where ξ is either r or z. In this manner, we can support the modeling of both radial and axial azimuthally symmetric coils. In either case, the electric field on this surface is a function only of ξ. The pitch of the coil is $P(\xi) = \tan\rho(\xi)$, where the pitch angle ρ is defined as the angle between the coil winding and the ξ axis. Our approach to implementing this model is to modify the electric field after it is advanced in time ($\mathbf{E}^0$) to zero its component parallel to the coil winding without modifying the component that is perpendicular. The parallel component of $\mathbf{E}^0$ is then

$$E_{\|}^0(\xi) = \mathbf{E}^0(\xi)\cdot\hat{\mathbf{p}}(\xi), \text{ where } \hat{\mathbf{p}}(\xi) = \cos\rho(\xi)\,\hat{\boldsymbol{\xi}} + \sin\rho(\xi)\,\hat{\boldsymbol{\theta}} \tag{D1}$$

is a unit vector parallel to the coil winding. From this, we obtain an expression for the corrected electric field by subtracting this parallel component from $\mathbf{E}^0$, i.e.,

$$\mathbf{E}^{cor}(\xi) = \mathbf{E}^0(\xi) - E_{\|}^0(\xi)\hat{\mathbf{p}}\,. \tag{D2}$$

Substituting (D1) into (D2), we obtain

$$E_\xi^{cor}(\xi) = E_\xi^0(\xi)\sin^2\rho(\xi) - E_\theta^0(\xi)\sin\rho(\xi)\cos\rho(\xi) = \frac{P^2(\xi)E_\xi^0(\xi) - P(\xi)E_\theta^0(\xi)}{1+P^2(\xi)} \tag{D3}$$

$$E_\theta^{cor}(\xi) = E_\theta^0(\xi)\cos^2\rho(\xi) - E_\xi^0(\xi)\sin\rho(\xi)\cos\rho(\xi) = \frac{E_\theta^0(\xi) - P(\xi)E_\xi^0(\xi)}{1+P^2(\xi)}\,. \tag{D4}$$

Quicksilver uses a standard Yee algorithm[3] for the spatial and temporal discretization of Maxwell's equation. In this algorithm discrete values of E_ξ and E_θ are collocated in time, but unfortunately are not collocated spatially. In the ξ direction, discrete values of E_ξ are located midway between E_θ values. Consequently, values of E_θ used in (D3), and values of E_ξ used in (D4) must be approximated in some fashion. The standard approach to deal with this issue, and the one that we have chosen, is to linearly interpolate the needed values from their bounding discrete locations. For a uniform grid, this reduces to using the mean of these two values. For a non-uniform grid, this becomes a weighted average, where the weights are a function of the grid index *i*, where $\{\xi_i\}$ represents the set of discrete locations of a given variable.

In the discussion so far, we have described a model for treating a surface of infinitesimal thickness. Due to the spatial discretization of the algorithm, this could reasonably be interpreted as a very thin volume whose thickness is comparable to the cell size in the direction (η) normal to the surface. However, actual coils will have thickness, which could in fact consist of many cells in the η direction, and modeling that thickness accurately could be important. In addition, with the addition of electrons (see the following section), a finite thickness of at least one cell is required to properly model electron-coil interactions. To address the need for thickness, we simply enforce (D3) and (D4) for every discrete η grid location that is either on the surface of, or interior to, the coil.

D.2. Interaction of 2D Coil Model with Simulation Electrons

There are issues related to the interaction of simulation electrons with our 2D coil EM model. In the presence of sufficient electric field, electrons will certainly be emitted from the individual coil windings. Also, any time an electron passes through the plane of the coil, it may or may not strike a winding, and its motion would be influenced by any local magnetic fields due to the individual windings. Models needed to be added to Quicksilver to address these issues.

It should be noted that since the 2D coil carries electric current, there will necessarily be a discontinuity in the magnetic field from one side of the coil to the other. Electromagnetically, due to the nature of the Yee algorithm, the code can resolve this discontinuity even if the coil has no thickness. However, for electrons in the vicinity of a zero-thickness 2D coil, this discontinuity is not resolved, and consequently the forces that accelerate the electron are not correct. To avoid this problem, the 2D coil must be at least one cell thick. Even in this case, the implementation of the 2D coil model must include adjusting the magnetic field in such a way that the particle sees a field that goes discontinuously to zero at the surface of the coil. This is the same modification that is required at conductor surfaces.

D.2.1. Electron Emission form 2D Coil Surfaces

Our studies have indicated that assuming a solid, perfectly-conducting surface for electron emission is adequate to model emission from coil surfaces. This is probably not surprising, since the pressure-balance-based theory of the operation of magnetically-insulated transmission lines (MITL) predict this, and in fact previous simulations have clearly demonstrated that there is

essentially no difference in the behavior of MITL's with uniform or "spotty" emission from their cathode surfaces.

Implementation of this model required some modifications to Quicksilver's approach to treating electron emission. For example, emission surfaces in Quicksilver are specified in terms of surfaces of conductors. The code needed to be modified to support alternate specification in terms of the surfaces of 2D coil models.

D.2.2. Electrons Entering the Volume of a 2D Coil

The simplest way to treat an electron passing through the volume of a 2D coil is to simply let it pass through unimpeded. Without any modifications to Quicksilver's standard algorithm, this effectively is what takes place. This was the first thing that we tried, and quickly learned that this was not satisfactory, producing a large, non-physical buildup of charge in the immediate vicinity of the coils. We have since devoted considerable effort to implementing and studying various methods of modeling particle/coil interaction, with the goal of determining the best methods in terms of capturing the real physical behavior of the actual device.

In actual coil system, one would expect only some fraction of the electrons passing through a coil to strike a winding and be "killed." To explore this issue, we have implemented a model that randomly "kills" a specified fraction, between zero and one, of the electrons that pass through a coil. Our first implementation suffered from significant errors in charge conservation. Although such errors do not in general indicate a problem, their presence does not bolster one's confidence in the algorithm. Consequently, significant effort was invested in modifications to make the algorithm charge-conserving. That effort was successful, and we believe that we are in fact properly modeling the coils as partially transparent to electrons. In exploring this model over the range of the kill-fraction parameter, we have discovered that the results are relatively insensitive to the value of this parameter. For example, for a typical simulation, measured currents vary by only a few percent when this factor varies from 0.5 to 1.0. If the lower end of the range is reduced to 0.1, the measured currents vary by less than ten percent. 3D simulations of current-carrying vane-like structures and electrons could be used to provide a better understanding of this interaction, but we consider it to be of relatively low priority because of the insensitivity of our results to this effect. For our simulations, we typically choose a "kill" fraction somewhat less than one.

1. M. E. Savage, D. B. Seidel, C. W. Mendel, Jr., "Design of a Command-Triggered Plasma Opening Switch for Terawatt Applications," *IEEE Trans. Plasma Science* **28**, 1533-1539, 2000.
2. J. P. Quintenz, D. B. Seidel, M. L. Kiefer, T. D. Pointon, R. S. Coats, S. E. Rosenthal, T. A. Mehlhorn, M. P. Desjarlais, and N. A. Krall, "Simulation Codes for Light-Ion Diode Modeling," Laser Part. Beams **12**, 283-324, 1994.
3. K. S. Yee, IEEE Trans. Antennas Propag. **14**, 302, 1966.

DISTRIBUTION

1 C. W. Mendel, Jr.
Cove Consulting
12449 Bending Stream Dr.
Bell Haven, VA 23306-1701

1	MS1152	M. Caldwell	1653
1	MS1152	R. S. Coats	1653
1	MS1152	R. E. Jorgenson	1653
1	MS1152	M. L. Kiefer	1652
1	MS1152	W. L. Langston	1654
1	MS1152	L. P. Mix	1654
1	MS1152	M. F. Pasik	1654
1	MS1152	T. D. Pointon	1654
5	MS1152	D. B. Seidel	1654
1	MS1152	L. K. Warne	1653
1	MS1181	D. H. McDaniel	1602
1	MS1181	L. X. Schneider	1650
1	MS1186	M. Herrmann	1680
1	MS1186	S. E. Rosenthal	1684
1	MS1186	S. A. Slutz	1684
1	MS1186	R. A. Vesey	1684
1	MS1189	M. P. Desjarlais	1640
1	MS1189	R. W. Lemke	1641
1	MS1189	T. A. Mehlhorn	1640
1	MS1190	M. K. Matzen	1600
1	MS1191	J. L. Porter	1670
1	MS1191	M. A. Sweeney	1670
1	MS1193	M. E. Cuneo	1683
5	MS1194	M. A. Savage	1671
1	MS1194	K. W. Struve	1670
1	MS1196	R. J. Leeper	1687
1	MS1196	W. A. Stygar	1671

1	MS0899	Technical Library	9536 (electronic copy)
1	MS0123	D. Chavez, LDRD Office	1011

Sandia National Laboratories